



HAL
open science

Behavior of critical metals in metamorphosed Pb-Zn ore deposits: example from the Pyrenean Axial Zone

Alexandre Cugerone, Bénédicte Cenki-Tok, Manuel Munoz, Kalin Kouzmanov, Emilien Oliot, Vincent Motto-Ros, Elisabeth Le Goff

► To cite this version:

Alexandre Cugerone, Bénédicte Cenki-Tok, Manuel Munoz, Kalin Kouzmanov, Emilien Oliot, et al.. Behavior of critical metals in metamorphosed Pb-Zn ore deposits: example from the Pyrenean Axial Zone. *Mineralium Deposita*, In press, 10.1007/s00126-020-01000-9 . hal-03026573v3

HAL Id: hal-03026573

<https://hal.science/hal-03026573v3>

Submitted on 25 Nov 2020 (v3), last revised 8 Oct 2021 (v4)

HAL is a multi-disciplinary open access archive for the deposit and dissemination of scientific research documents, whether they are published or not. The documents may come from teaching and research institutions in France or abroad, or from public or private research centers.

L'archive ouverte pluridisciplinaire **HAL**, est destinée au dépôt et à la diffusion de documents scientifiques de niveau recherche, publiés ou non, émanant des établissements d'enseignement et de recherche français ou étrangers, des laboratoires publics ou privés.

Article

Behavior of critical metals in metamorphosed Pb-Zn ore deposits: example from the Pyrenean Axial Zone

Alexandre Cugerone,¹ 
Email alex.cugerone@gmail.com

Bénédicte Cenki-Tok,^{1,2}
Email benedicte.cenki-tok@umontpellier.fr

Manuel Muñoz,¹
Email manuel.munoz@umontpellier.fr

Kalin Kouzmanov,³
Email Kalin.Kouzmanov@unige.ch

Emilien Oliot,¹

Email emilien.oliot@umontpellier.fr

Vincent Motto-Ros,⁴

Email vincent.motto-ros@univ-lyon1.fr

Elisabeth Le Goff,⁵

Email e.legoff@brgm.fr

¹ Géosciences Montpellier, Université de Montpellier, CNRS, Montpellier, France [AQ1](#)

² Earthbyte Research Group, School of Geosciences, University of Sydney, Sydney, NSW, 2006 Australia

³ Department of Earth Sciences, University of Geneva, Geneva, Switzerland

⁴ Institut Lumière Matière Université Lyon 1, Villeurbanne, France

⁵ BRGM, Bureau de Recherches Géologiques et Minières, Montpellier, France

Received: 27 July 2019 / Accepted: 15 June 2020

Abstract

Rare metals (Ge, Ga, In, Cd) are key resources for the development of green technologies and are commonly found as trace elements in base-metal mineral deposits. Many of these deposits are in orogenic belts and the impact of recrystallization on rare metal content and distribution in sphalerite needs to be evaluated. Based on laser ablation inductively coupled plasma mass spectrometry (LA-ICP-MS) analyses, and micro-imaging techniques such as laser-induced breakdown spectroscopy (LIBS) and electron backscattered diffraction (EBSD), we investigate the minor and trace element composition related to sphalerite texture for three types of mineralization from the Pyrenean Axial Zone (PAZ). Vein mineralization (type 2b) appears significantly enriched in Ge and Ga compared to disseminated and stratabound mineralization (type 1 and type 2a, respectively). In vein mineralization, the partial recrystallization induced by deformation led to the remobilization of Ge, Ga, and Cu from the sphalerite crystal lattice into accessory minerals. We propose that the association of intragranular diffusion and fluid-rock reaction were likely responsible for the formation of patchy-oscillatory zoning in

sphalerite, and the crystallization of Ge-rich accessory minerals. Chemical and textural heterogeneity is common in sphalerite from various world-class deposits and a full understanding of these heterogeneities is now crucial to assess the rare metal potential, and associated extraction processes of deformed base-metal ores.

Editorial handling: H. A. Gilg

Electronic supplementary material

The online version of this article (<https://doi.org/10.1007/s00126-020-01000-9>) contains supplementary material, which is available to authorized users.

Introduction

Sphalerite (ZnS) commonly contains high amounts (up to a few 1000s of ppm) of rare metals such as germanium (Ge), indium (In), gallium (Ga), or cadmium (Cd), which are currently extracted as by-products from zinc concentrates (Frenzel et al. 2014, 2016, 2017; Licht et al. 2015) and considered critical for the economy (European Commission 2017; U.S. Geological Survey 2019). These high concentrations of trace elements are generally related to undeformed sphalerite in the form of coarse crystals originating from open-space crystallization or from colloform-banded precipitates with fine-grained textures (Cerny and Schroll 1995; Goffin et al. 2015; Henjes-Kunst et al. 2017; Cugerone et al. 2018a). Undeformed sphalerite occurs mainly in Mississippi Valley type (MVT) and polymetallic vein deposits (Viets et al. 1992; Saini-Eidukat et al. 2009; Murakami and Ishihara 2013; Belissont et al. 2014; Bonnet 2014; Bauer et al. 2018). However, the largest sphalerite deposits are found in orogenic domain (Lawrence 1973; Moore et al. 1986; Kelley and Jennings 2004; Kampunzu et al. 2009; Wilkinson 2013; Gibson et al. 2017). This reflects the fact that the ores originally formed as sediment-hosted massive sulfide (SHMS), volcanic-hosted massive sulfide (VHMS), or carbonate-hosted deposits (Kipushi-type, more rarely MVT) are more likely to have undergone metamorphism and recrystallization during an orogenic event (Bernstein and Cox 1986; Hughes 1987; Murphy 2004; Wagner and Monecke 2005; Huston et al. 2006; Melcher et al. 2006; Monteiro et al. 2006; Kamona and Friedrich 2007; Reiser et al. 2011; Ye et al. 2011).

In metamorphic environments, remobilization of minor and trace elements related to dynamic recrystallization, annealing, or even brecciation has been studied for various sulfide minerals. The mobility of Au, As, Ni, Co, Pb, Bi, and Se has been examined in pyrite (Cook et al. 2009a; Large et al. 2009; Reddy and

Hough 2013; Velásquez et al. 2014; Dubosq et al. 2018; Kampmann et al. 2018), arsenopyrite-löllingite (Tomkins and Mavrogenes 2001; Wagner et al. 2007; Fougereuse et al. 2016) and pyrrhotite (Vukmanovic et al. 2014). The dynamic recrystallization assisted by metamorphic fluids in gold systems releases invisible gold from the sulfide crystal lattice and subsequent crystallization of metallic gold (Fougereuse et al. 2016; Dubosq et al. 2018). Lockington et al. (2014) studied sphalerite mineralization from metamorphosed VHMS and SHMS deposits. Metamorphic recrystallization was shown to lead to remobilization of minor and trace elements resulting in a loss of compositional zoning, and homogenization of Cu distribution in the crystal lattice of sphalerite, possibly associated to a depletion in Pb, Bi, and Ag and an enrichment in Fe, Cd, Mn, and In. These data were acquired in various deposits of different metamorphic grade and the role of primary enrichment for these elements cannot be clearly established. In Neves-Corvos (Iberian Pyrite Belt, Carvalho et al. 2018), indium is primarily incorporated in high-temperature sphalerite and chalcopyrite, but was not lost during recrystallization associated to hydrothermal re-working and/or low-grade tectonometamorphic overprints (Relvas et al. 2006; Carvalho et al. 2018). Nonetheless, roquesite (CuInS_2) locally occurs at sulfide grain boundaries. In sphalerite from Neves Corvo, Ge is reported below ~ 100 ppm Ge (Carvalho et al. 2018). In the Barrigão deposit (Iberian Pyrite Belt), Reiser et al. (2011) and Belissont et al. (2019) suggested late-stage remobilization of germanium associated to low-grade metamorphism (260–300 °C) with germanium enrichments in chalcopyrite and accessory phases localized in fractures. Cugerone et al. (2020) showed evidence for redistribution of Ge in partly recrystallized sphalerite from the Arre vein deposit (Pyrenean Axial Zone). Recrystallized sphalerite is Ge-depleted but correspond to textures where Ge minerals occur, compared to dark domains in coarser grains which still contain up to ~ 600 ppm Ge in the sphalerite lattice. Occurrences of rare metals such as Ge, Ga, In, and Cd within deformed/metamorphosed sphalerite ore remain poorly documented and their behavior in such systems needs to be evaluated.

AQ2

Sphalerite is ductile at relatively low temperature in various experimental deformation studies (< 400 °C; Clark and Kelly 1973; Siemes and Borges 1979; Couderc et al. 1985; Cox 1987). No experimental study on the impact of sphalerite deformation on trace elements behavior is available.

Currently, the production of rare metals from base-metal deposits remains challenging. Germanium is generally extracted, for example, by hydrometallurgy followed by various mass transfer techniques (Ruiz et al. 2018). However, only a few percent of the total rare metal content in sphalerite (at ppm level) is

recovered due to a negative effect which prevents the extraction of zinc (around ~ 3% of the Ge extracted; Ruiz et al. 2018; U.S. Geological Survey 2019). Chemical extraction from highly concentrated phases (with Ge contents > 1 wt%), previously separated by magnetic or mechanic techniques, could prove to be much more profitable (Cugerone et al. 2019).

This study aims to decipher the behavior of rare metals, mainly Ge, Ga, In, and Cd, in sphalerite from different Pb-Zn deposits and mineralization styles of the Pyrenean Axial Zone (PAZ). The Pb-Zn deposits of the PAZ contain sphalerite rich in rare metal (ppm level) and Ge-rich accessory minerals, such as brunogeierite GeFe_2O_4 , briartite $\text{GeCu}_2(\text{Fe}, \text{Zn})\text{S}_4$, carboirite $\text{GeFeAl}_2\text{O}_5(\text{OH})_2$, or argutite GeO_2 (Laforet et al. 1981; Johan et al. 1983; Bernstein 1985; Johan and Oudin 1986; Pouit and Bois 1986; Julliot et al. 1987; Cugerone et al. 2018a). We have investigated the textural and chemical composition of different types of sphalerite mineralization in the Pyrenees using an in situ quantitative analysis by LA-ICP-MS and micro-imaging techniques such as EBSD and LIBS mapping. We show a detailed genetic model at vein and granular scales for the partitioning of Ge and associated trace elements between sphalerite and accessory minerals. Finally, we present a comparison with other Ge-enriched Pb-Zn deposits worldwide.

Sampling and analytical methods

Oriented ore samples were collected from underground mines or surface outcrops. We have studied polished sections (either 30 or 150 μm thick) from six Pb-Zn deposits of three mineralization types.

EBSD analysis is used to characterize the texture and the grain size of the sphalerite. This technique requires a well-polished surface. In order to eliminate surface defects, a last step of polishing (0.25 μm) was performed using a Vibromet polisher with 150 g of pressure on a polyurethane layer with colloidal silica. During this process, cleaning the frozen colloidal silica was necessary to avoid scratches on sphalerite. EBSD maps were performed with a Camscan Crystal Probe X500FE SEM-EBSD at Geosciences Montpellier (CNRS-University of Montpellier, France). Operating conditions were 20 kV and 5 nA, with a working distance of 25 mm under 2 Pa low vacuum. Sample surfaces were positioned horizontally at 20° to the incident electron beam to improve the collection of the backscattered electrons. Element distribution maps and backscattered electron (BSE) images were simultaneously acquired by measuring X-ray fluorescence with an EDS (energy-dispersive spectrometer). The step size for 2D imaging was below 5 μm . EBSD mapping was preferentially performed on sphalerite, indexed as a cubic crystal symmetry,

while Ge minerals were localized by EDS maps. The EBSD indexation of quartz, calcite, galena, and pyrite was also performed. Match units used for sphalerite indexation were derived from published crystallographic data from Villars and Calvert (1991). The lower misorientation limit for grain boundary indexation is fixed at 20° following careful investigation on misorientation boundary maps superposed on orientation maps. Oxford Instruments softwares AZtec and Channel 5 were used to generate maps using the EDS (chemical maps) and EBSD (structural maps).

Electron probe micro-analyses were carried out using a Cameca SX100 at the Service Inter-Régional Microsonde-Sud (Montpellier, France). Major, minor, and trace elements were measured with a beam current of 100 nA and accelerating voltage of 20 kV. The analytical procedure and detailed settings for each elemental analysis are detailed in Cugerone et al. (2018a). Zinc concentrations of sphalerite crystals were used as an internal calibration for LA-ICP-MS analyses.

LA-ICP-MS was used to determine minor and trace element concentrations in sphalerite. Type 1 sphalerite was analyzed in one sample from Bentaillou ($n = 7$), type 2a sphalerite in three samples from Bentaillou ($n = 12$), Margalida ($n = 9$), and Victoria ($n = 11$). Type 2b sphalerite was measured in three samples from Arre ($n = 36$), Anglas ($n = 40$), and Pale Bidau ($n = 30$).

Analyses were carried out using an Excimer CompEx 102 coupled to a ThermoFinnigan Element XR at the OSU-OREME AETE platform (University of Montpellier, France). Laser ablation was performed using a constant 5 Hz pulse rate at 140 mJ with a spot diameter of 26 μm . Each analysis comprises 180 s of background measurement and 60 s of sample ablation (signal measurement), followed by a 60-s retention time to ensure a proper cell washout. Data were processed using the Glitter 4.0 software package (Van Achterbergh et al. 2001). The following isotopes were measured: ^{29}Si , ^{34}S , ^{55}Mn , ^{57}Fe , ^{59}Co , ^{61}Ni , ^{63}Cu , ^{64}Zn , ^{69}Ga , ^{74}Ge , ^{75}As , ^{77}Se , ^{95}Mo , ^{105}Pd , ^{107}Ag , ^{111}Cd , ^{115}In , ^{118}Sn , ^{121}Sb , and ^{208}Pb . MASS-1 reference material (Wilson et al. 2002) was used as an external standard with a corrected 57 ± 1.75 ppm value for Ge (Dr. Stephen Wilson, personal communication). NIST SRM 610 (Pearce et al. 1997) was used as secondary external standard to identify possible instrumental drift. Concentrations for Ni, As, Mo, Se, Pd, and Si were below detection limits in all measurements. Several time-integrated LA-ICP-MS spectra are reported in the electronic supplementary material (ESM 1), illustrating the time intervals used for the measurements. One standard deviation is systematically indicated for median values.

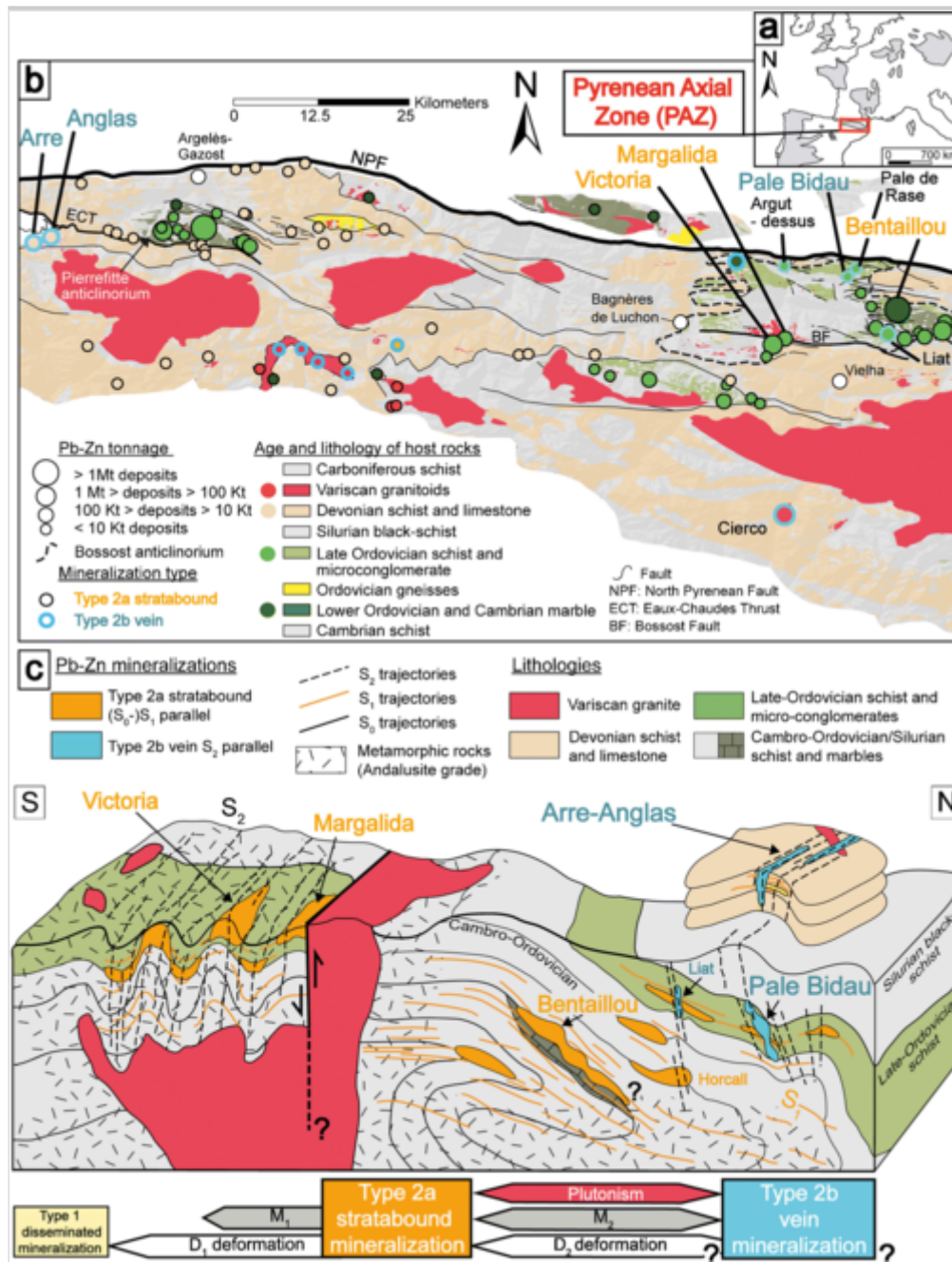
Laser-induced breakdown spectroscopy (LIBS) imaging technique was used to highlight the distribution of Ge, Cu, Ga, Zn, Si, Fe, Cd, Al, Mg, and Ti, in a highly zoned sphalerite sample from Arre (ARR03 sample) to map metallic elements at a micrometric spatial resolution, and with a sensitivity at the ppm level (Sancey et al. 2014; Cáceres et al. 2017; Fabre et al. 2018). During the analysis, the sample surface is scanned, through single laser pulses, in a pixel-by-pixel manner to induce the breakdown of the material. The light radiation emitted by the plasma is then collected by an optical system and analyzed using a spectrometer. The sample was excited using Nd:YAG laser with a pulse energy of about 600 μJ operating at 100 Hz and a lateral resolution (i.e., distance between two consecutive laser shots) of 13 μm . The surface analyzed is about 6 cm^2 (3.6 megapixels) and was measured in 6 h. The spectrometer was configured in the spectral range 250–330 nm to detect Ge (265.1 nm), Cu (324.7 nm), and Ga (294.4 nm). Due to an interference with Al, the Ge line at 269.1 nm was used in the aluminosilicate phases.

Geological setting

The Pb-Zn ore deposits are hosted in the Variscan PAZ (Fig. 1a) and exhumed during the Paleogene collision between the Iberia and Eurasian plates (Zwart 1979; Carreras and Druguet 2014). The PAZ is composed of Paleozoic metasediments intruded by Ordovician and Late-Variscan granite (Fig. 1b; Kleinsmiede 1960; Zwart 1963; Denèle et al. 2014). The Pb-Zn deposits are concentrated in pluri-kilometric structures such as the Bossost or Pierrefitte anticlinoria (Fig. 1b).

Fig. 1

a Location of the Pyrenean Axial Zone in the Variscan belt of Western Europe. **b** Lithological and structural map of Central Pyrenean Axial Zone with location of Pb-Zn deposits (from Pouit 1985, Bureau de Recherches Géologiques et Minières [<http://infoterre.brgm.fr>], and Instituto Geológico y Minero de España [<http://mapas.igme.es/Servicios/default.aspx>]). **c** Structural 3D synthetic model with location of the studied Pb-Zn deposits in relation to lithology, structure, and metamorphic grade. Chronological interpretation from Cugerone et al. (2018b). Timing of mineralization for the type 2b vein mineralizations is unknown but deformation imprint is considered as Late-Variscan (D_2)



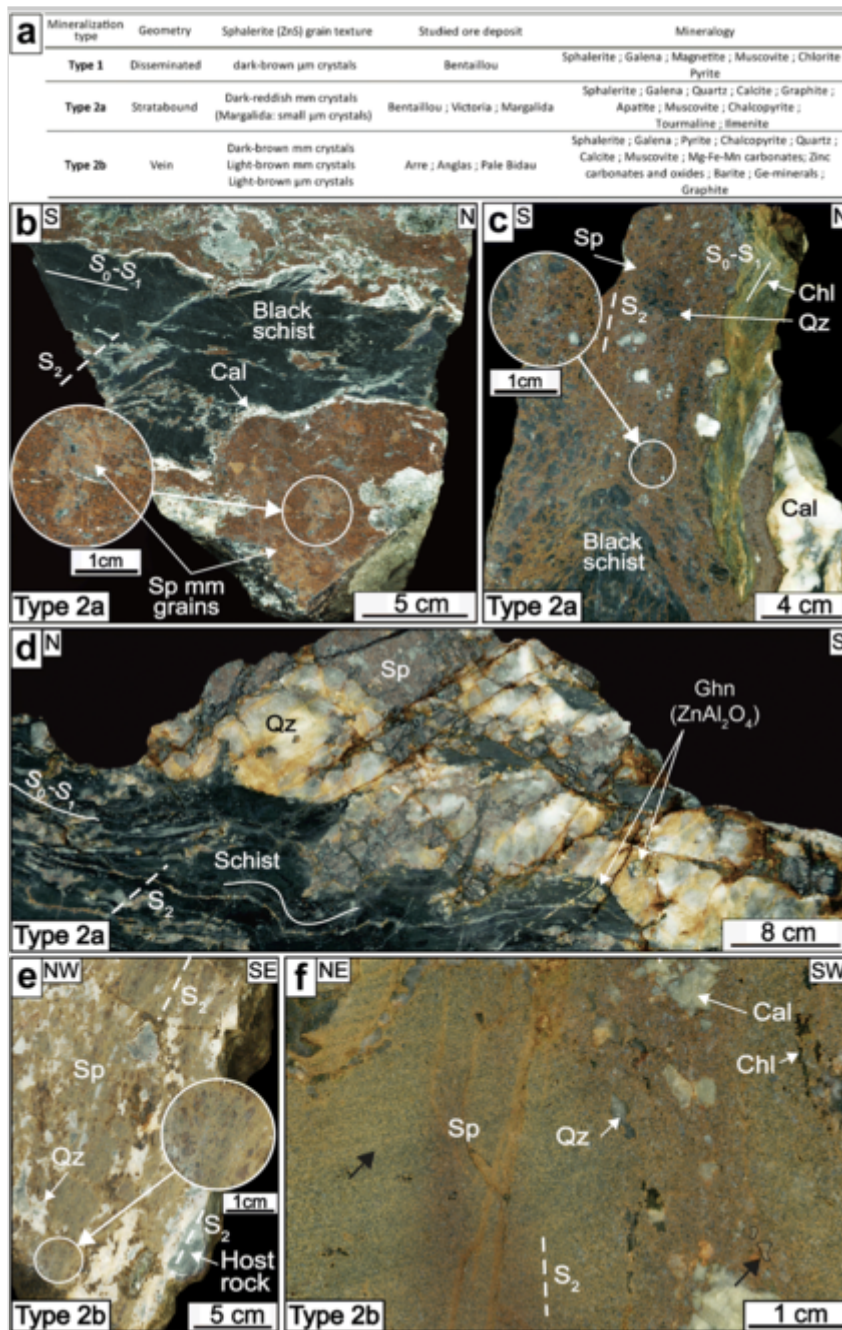
The Pb-Zn district of the PAZ was exploited in twentieth century. It has produced ca. 400 kt of Zn and 180 kt of Pb (BRGM 1984; Ovejero Zappino 1991). Three types of Pb-Zn mineralization are described in Cugerone et al. (2018b). Type 1 is minor, disseminated, and laminated mineralization, probably associated to sedimentation during Cambro-Ordovician and Devonian times (Fig. 1c). Type 2a is a structurally controlled mineralization parallel to S_0 - S_1 (Fig. 1c), synchronous to Variscan D_1/M_1 regional deformation/metamorphism related to crustal thickening (Zwart 1963, 1979; Mezger et al. 2004; Laumonier et al. 2010) with a peak estimated at 580 °C and 0.55 GPa in the Bossost dome (Mezger et al. 2004). Type 2a mineralization pre-dates Variscan M_2 contact metamorphism, culminating at ca. 525 °C and 0.2 GPa (Mezger and Passchier 2003; Mezger et al. 2004; de Hoÿm de Marien et al. 2019) in the Victoria-

Margalida area. In the field, type 2a mineralization appears in metric pull-apart type structures in Cambrian marble as in Bentaillou (Fig. 1c) or folded by D_2 deformation in Late-Ordovician metasediments in Victoria (Fig. 1c). It can also be associated to fault damaged zones in Late-Ordovician marble in Margalida (Fig. 1b; Cugerone et al. 2018b).

Type 2b (Fig. 1) is epigenetic vein mineralization probably late, or post-dating, the D_2/M_2 deformation event (Cugerone et al. 2018b). Pb-Zn mineralization is structurally controlled and occurs as vertical decimetric-sized veins parallel to S_2 cleavage, which locally intersect type 2a mineralization. No alteration halo has been observed along the contact with the host-rock. Type 2b mineralization cuts Late-Variscan aplitic intrusions and is affected by a cleavage parallel to the Late-Variscan S_2 cleavage in the host rock (Cugerone et al. 2018b). We have studied samples from type 2b Pale Bidau, Arre, and Anglas deposits hosted in calc-schists (Fig. 2b). A late D_3 deformation is reported in the literature (Carreras and Druguet 2014; Cochelin et al. 2017) and corresponds to faults like the Bossost mylonitic fault close to type 2a Margalida deposit.

Fig. 2

Polished samples of type 2a and type 2b mineralization (Cal: calcite; Chl: chlorite; Ghn: gahnite; Qz: quartz; Sp: sphalerite). **a** Characteristic of the three mineralization types: type 1, type 2a, and type 2b. **b** Sample with millimetric coarse-grained sphalerite (dark brown reddish), associated to calcite (white), and black-schist (Bentaillou deposit). **c** Pluri-micrometric small-grained sphalerite (dark brown reddish). A brecciated texture can be observed with clasts of quartz, calcite, and black-schist (Margalida deposit). **d** Folded (F_2) coarse-grained sphalerite and quartz mineralization. Gahnite crystals are reported in schists and in the mineralization (Victoria deposit). **e** Light to dark brown zonation in sphalerite crystals associated to quartz and calc-schist host rock. Set shows coalescence of coarse millimetric and small micrometric crystals appear (Arre deposit). **f** Light to dark brown sphalerite associated to quartz, calcite, and chlorite. Dark brown vertical bands are visible on the sample. Sphalerite grains are locally visible as shown by the black arrow at bottom right (Pale Bidau deposit)



Results

Mineralization types and textures

The three types of mineralization are mainly composed of sphalerite and galena, with minor pyrite, chalcocopyrite, arsenopyrite, and gangue of quartz-carbonate (Fig. 2a).

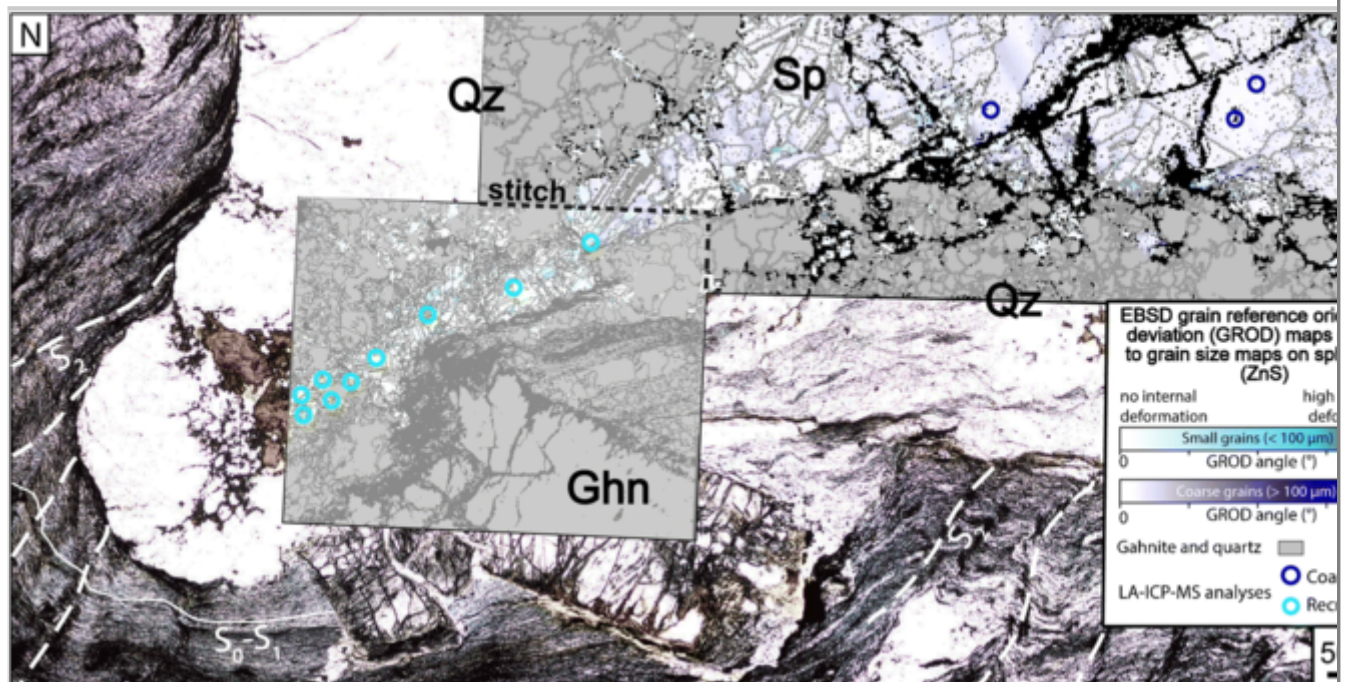
Type 1 is composed of micrometric-size disseminated sulfide crystals. This mineralization is crosscut by type 2a veins (Bentailou deposit; Cugerone et al. 2018b). It consists of pluri-micrometric euhedral dark brown crystals.

Type 2a sphalerite shows undeformed millimeter-size twinned crystals and polygonal shape that is dark-red in polished slabs (Fig. 2b). The texture is

different at Margalida (Fig. 2c), which presents micrometer-scale dark brown sphalerite grains and forming the matrix of a *durchbewegung* breccia composed of quartz, calcite, and schist clasts. Sphalerite is folded in Victoria (Fig. 2d) and cross-cuts metamorphic centimeter-scale gahnite (Fig. 3; Cugerone et al. 2018a). Sphalerite exhibits recrystallized textures in F_2 fold hinges (Fig. 3).

Fig. 3

EBSD-grain reference orientation deviation angle component (GROD) maps related to grain size superimposed onto a transmitted-light microphotograph of type 2a sphalerite-quartz mineralization hosted in schist deformed by F_2 fold hinge from Victoria deposit. The GROD maps allow to visualize intragranular microstructures and represent the misorientation deviation for each pixel compared to the mean misorientation deviation of the entire sphalerite grain (steps of measurement of 4 and 10 μm for the left and right EBSD maps respectively). In the GROD calculation, twin boundaries are considered as grain boundaries to exclude their large misorientation ($55\text{--}60^\circ$) (Ghn: gahnite; Qz: quartz; Sp: sphalerite). LA-ICP-MS spot analyses in type 2a coarse and recrystallized sphalerite are indicated



The mineral assemblages of types 2a and 2b veins (Cugerone et al. 2018b) are distinct with the presence of apatite, ilmenite, and tourmaline in type 2a and Gem minerals, graphite, and Mg-Fe-Mn-Zn carbonates in type 2b. Sphalerite crystals of type 1, 2a, and 2b mineralizations do not contain chalcopyrite inclusions.

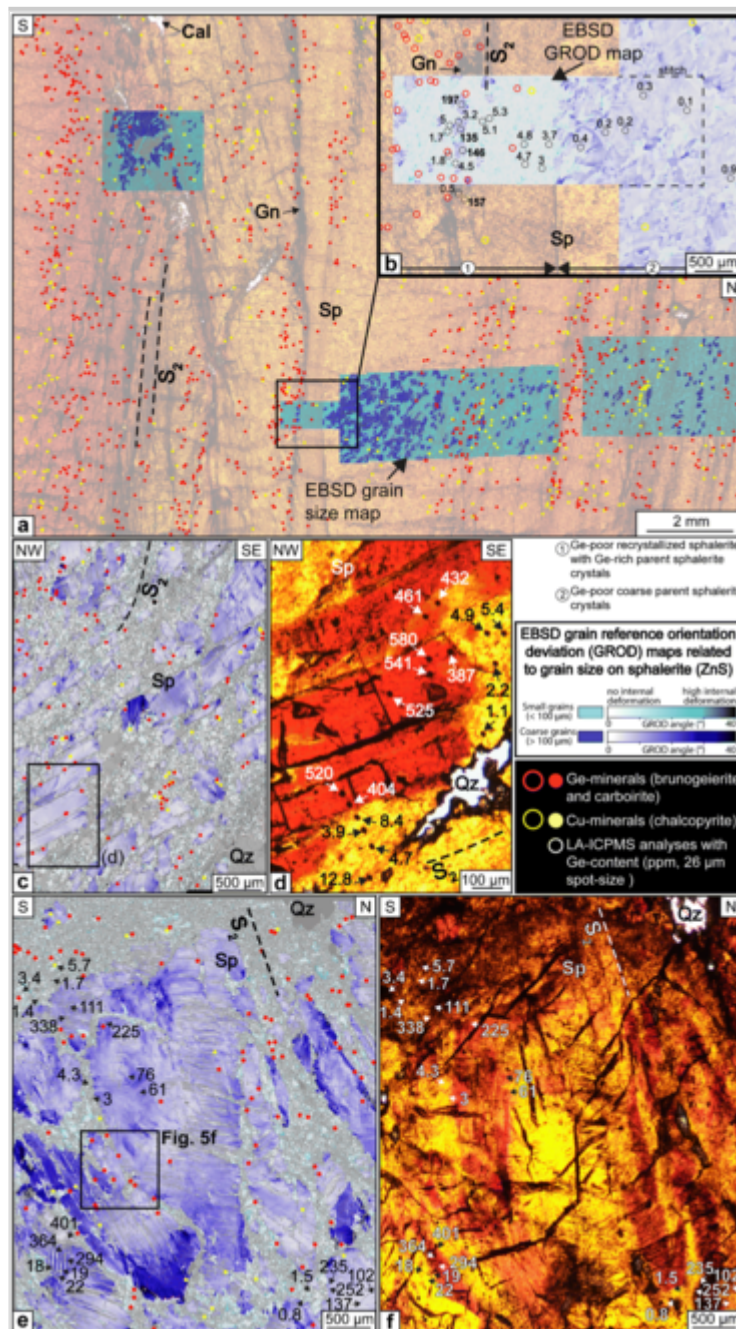
Type 2b sphalerite is light to dark brown in transmitted-light and with heterogeneous grain size resulting from a superimposed cleavage (considered to

be S_2) parallel to the vein contact (Fig. 2e and f). In the Arre, Anglas, and Pale Bidau deposits, sphalerite crystals exhibit various colors from dark brown zones in coarse, millimetric grains, to light-brown zones in coarse millimetric, or fine micrometric, grain fractions (Figs. 2e and 3f). Quartz and carbonate show comb textures with the occurrence of cockade breccia mainly in Arre and Anglas type 2b veins. EBSD-grain reference orientation deviation (GROD) maps and transmitted-light microphotographs are superposed in Fig. 4. Coarse grains ($> 100 \mu\text{m}$) and small recrystallized grains ($< 100 \mu\text{m}$) are colored in shaded of dark and light blue, respectively. Blue colors are more pronounced where internal deformation is more intense. Three types of sphalerite textures appear in type 2b mineralization: coarse grains with dark brown domains, coarse grains with light-brown domains, and recrystallized light-brown crystals. Sub-vertical fine recrystallized fraction domains appear mostly in white color in the GROD maps (Fig. 4a) which attests to poor internal deformation and commonly mark the cleavage, for example in PB (Fig. 4a and b). Coarse crystals ($> 100 \mu\text{m}$) with color zones from light to dark brown are reported in the Arre and Anglas samples (Fig. 4c–f) and commonly contain ductile deformation attested by intense dark-blue color mainly close to grain boundaries (Fig. 4e). In the EBSD-GROD and the grain size maps, it is possible to discriminate between recrystallized and light-brown coarse grains while these two fractions show the same light-orange color in transmitted light (Fig. 4). Sphalerite from the Pale Bidau deposit exhibits blurred color domains with progressive variations from light to dark brownish tints and no intragranular color zonation is observed, especially in coarse grains.

Fig. 4

Microphotographs associated to EBSD-grain reference orientation deviation angle component (GROD) maps related to sphalerite grain size. The GROD maps allow to visualize intragranular microstructures. Small grains contain low internal misorientation compared to coarse grains, which confirm the presence of dynamic recrystallization. Grain boundaries are represented in all maps except in **b** and chemical contents acquired with LA-ICP-MS are reported (Gln: galena; Qz: quartz; Sph: sphalerite). **a** Scanned microphotograph of sphalerite with superposition of four EBSD-grain size maps (Pale Bidau deposit; step of measurements between 1.5 and 4 μm). Germanium and Cu minerals observed with EDS map are reported. Location of **b** is indicated. **b** Enlargement of **a** showing the location of LA-ICP-MS spot analyses with Ge contents essentially on two EBSD-GROD maps. Occurrence of Ge and Cu minerals are reported with empty yellow and blue circles to highlight relationships between Ge-Cu minerals and sphalerite (step of measurement of 1.5 and 4 μm for the left and right EBSD maps respectively). **c** EBSD-GROD map with location of Ge- and Cu-rich phases (Arre deposit). These minerals are preferentially located in the recrystallized sphalerite

domains. Location of **d** is represented (step of measurement of 2.5 μm). **d** Enlargement of **c** in transmitted-light with LA-ICP-MS spot analyses associated to Ge contents. Note that the color zonation correspond in part to variations in Ge content. **e** EBSD-GROD map with location of Ge- and Cu-rich minerals in recrystallized sphalerite (Anglas deposit). LA-ICP-MS spot analyses are located with their corresponding Ge contents (step of measurement of 3 μm). **f** Enlargement of **e** in transmitted-light (150 μm of thickness) with color zonation between light and dark brown. LA-ICP-MS spots are indicated with black or white arrows corresponding to **e**



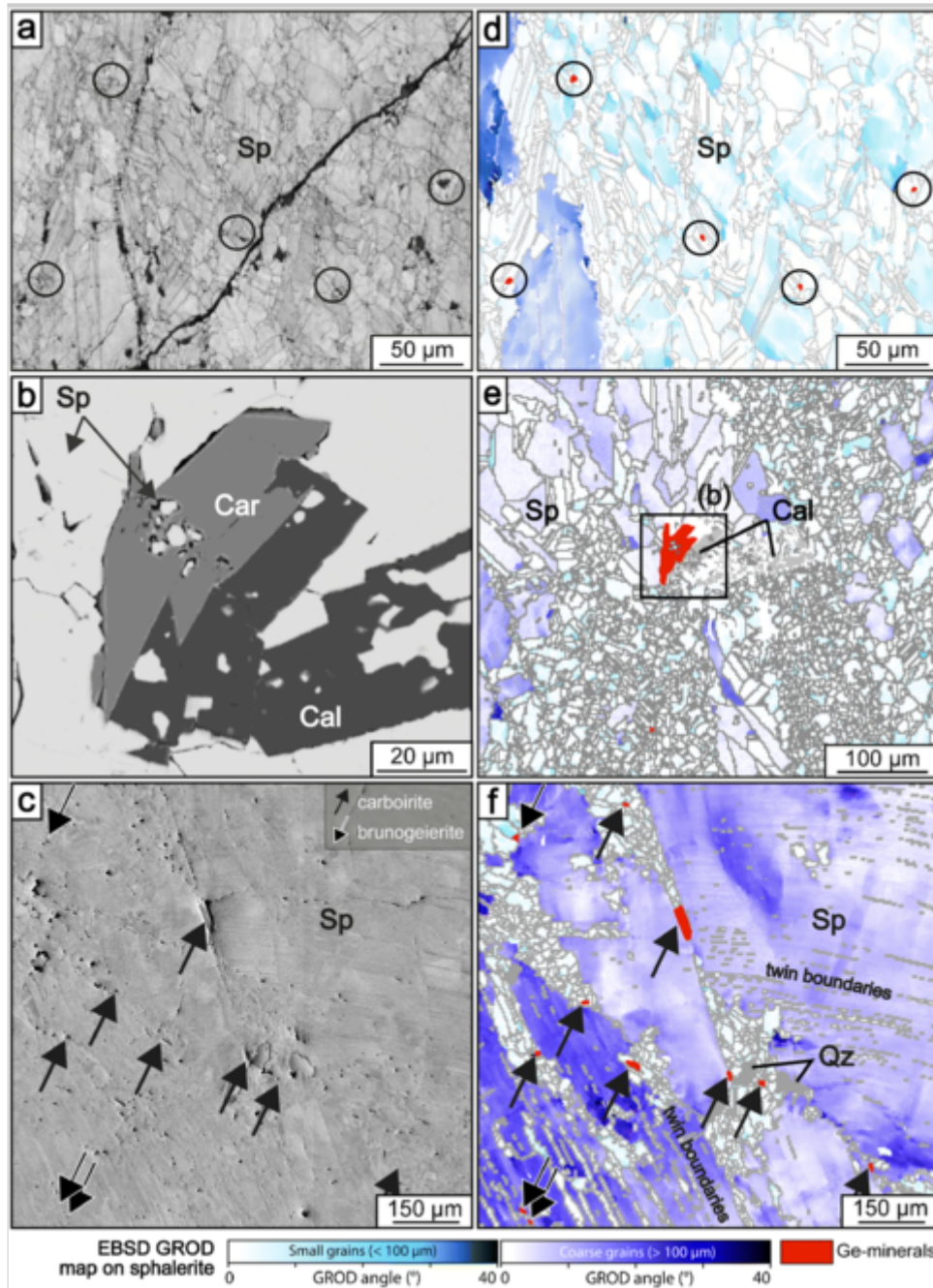
Minerals in which Ge is a major element have been identified by optical microscopy and EDS maps as brunogeierite (GeFe_2O_4), carboirite [$\text{FeA}_{12}\text{GeO}_5(\text{OH})_2$], briartite [$\text{Cu}_2(\text{Fe}, \text{Zn})\text{GeS}_4$], and argutite (GeO_2). Briartite

is the main Ge-mineral in Arre sphalerite but is rare in Anglas and Pale Bidau sphalerite. Carboirite, brunogeierite, and more rarely argutite are the common Ge-minerals in the Anglas and Pale Bidau deposits. These minerals are preferentially hosted along grain boundaries of recrystallized sphalerite grains. In Figs. 4 and 5, Ge-minerals occur as small crystals ($< 100 \mu\text{m}$; see yellow dots in Fig. 4) and are preferentially aligned in the S_2 cleavage. Similarly, micrometric chalcopyrite is preferentially aligned in the same recrystallized areas (Fig. 4). These minerals are detected in all type 2b samples (Fig. 4c and e). Carboirite crystals are coarser (from 10 to $100 \mu\text{m}$) compared to brunogeierite, argutite, and briartite (5 to $20 \mu\text{m}$ in size; Fig. 5). Figure 5a–c shows three representative examples of Ge-minerals occurrence characteristic of type 2b mineralization. Two sphalerite grain size fractions (below and above $100 \mu\text{m}$) are considered for the GROD maps (Fig. 5d–f). These maps show that Ge-minerals are only hosted between recrystallized sphalerite grains ($< 100 \mu\text{m}$, Fig. 5d and e) in areas with low GROD angle, at the contact or between coarse-grained sphalerite crystals or in twin boundaries (Fig. 5f).

Fig. 5

Images of Ge-minerals hosted in the interstices between recrystallized sphalerite grains (Cal: calcite; _____ one abbreviation is missing in the caption of the Figure 5 (visible on 5B): Car: Carboirite

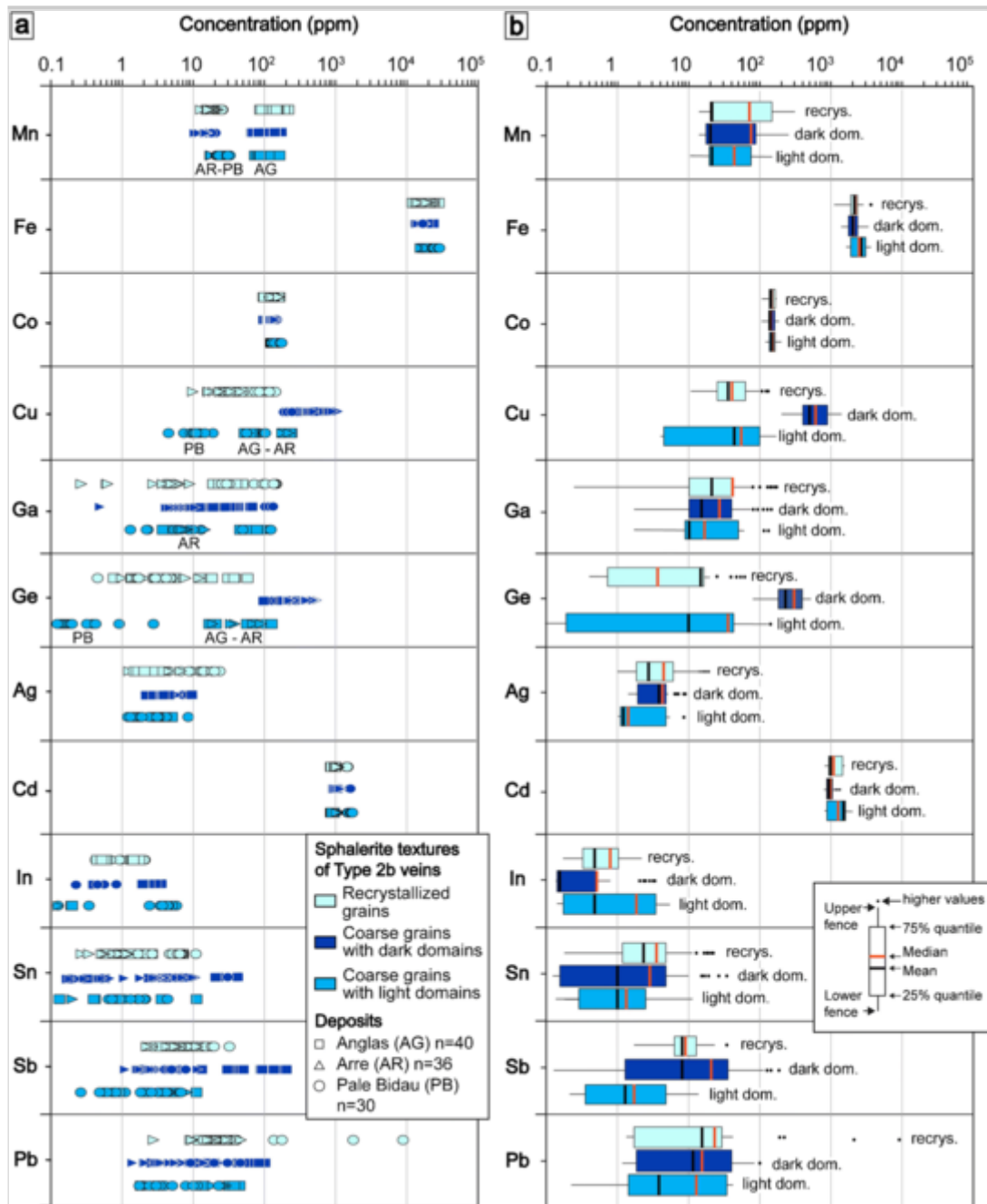
It will be: (Cal: calcite; Car: Carboirite; Qz: quartz; Sp: sphalerite) _____ Qz: quartz; Sp: sphalerite). **a** Five brunogeierite crystals from the Arre deposit (in the black circle; BSE image). **b** Carboirite crystals associated with into sphalerite and calcite from the Pale Bidau deposit (SEM image) **c** Nine Ge-minerals hosted between sphalerite grains from the Anglas deposit. **d–f** EBSD-GROD maps related to grain size for **a**, **b**, and **c**, respectively (step of measurement of 0.5, 3, and $3 \mu\text{m}$ for the three EBSD maps, respectively)



Chemical composition of sphalerite

The distribution of trace elements for type 1, 2a, and 2b mineralizations is plotted in the Figs. 6 and 7 (see dataset in ESM 1). The main characteristic of type 1 and type 2a sphalerite mineralizations is the small amount of Ge, mostly below 1 ppm (Fig. 6). In type 1 disseminated grains from Bentailou, Fe median content is 2.5 ± 0.2 ppm, and the concentrations of Cu and Ga are low with median values of 24 ± 22 ppm and 12 ± 1 ppm, respectively (Fig. 6). Variations in concentration are relatively large in Cu, Ga, Ag, Sn, Sb, and Pb compared to Fe, Co, Ag, or Cd with only minor disparities (Fig. 6).

Fig. 6



In type 2a, Fe median content is higher than that in type 1, with median value of 5.4 ± 0.5 ppm. Copper and Ga contents are generally low with values below 70 and 30 ppm and median contents of 11 ± 13 ppm and 1.4 ± 6 ppm, respectively (Fig. 6). Recrystallized grains in Victoria type 2a mineralization show lower median contents in Mn, Fe, Co, Ga, and Cd but higher median values in Ag, Pb, Sb, and Sn, compared to coarse grains in the same sample from Victoria (Fig. 6; analyzed spot locations are reported in Fig. 3). Recrystallized grains from Victoria and Margalida have similar Mn, Co, and Cu contents (Fig. 6) but Fe and Cd median values are distinct with 2.6 ± 0.1 wt% and 952 ± 20 ppm for Victoria recrystallized grains and 5.0 ± 0.4 wt% and 1946 ± 42 ppm for Margalida recrystallized grains (Fig. 6). Silver, Sn, Sb, and Pb concentrations are similar between Victoria and Bentailou coarse grains compared to Mn, Co, Cu, Ga, and Cd contents that show large variations (Fig. 6). For Bentailou coarse grains,

median values are 282 ± 19 ppm for Mn, 3.8 ± 0.2 wt% for Fe, 94 ± 7 ppm for Co, 1 ± 0.3 ppm for Ga, and 2246 ± 35 ppm for Cd. Manganese content is generally high in Victoria and Bentaillou coarse grains (Fig. 6) with median values of 289 ± 100 ppm. Cobalt content is high in Victoria coarse grains with a median value of 172 ± 10 ppm compared to the grains analyzed in other textural position that yield a median value of 89 ± 8 ppm. Cadmium is highly variable according to deposit and texture. Recrystallized Victoria coarse grains show the lowest contents with a median value of 956 ± 20 ppm (Fig. 6). Victoria coarse grains present higher Cd content with 1504 ± 28 ppm. But recrystallized grains from Margalida contain similar Cd values with median contents of 1557 ± 37 ppm. Indium content is generally below detection limit, when detected the median value is 0.8 ± 0.4 ppm. Silver, Sn, Sb, and Pb contents are generally higher in recrystallized grains (and in type 1 disseminated crystals) than in coarse grains (Fig. 6). In addition, Ag contents are relatively low with total median value of 7 ± 3 ppm but locally, Ag can reach 43 ppm in Margalida sphalerite (Fig. 6). The same range of concentrations is observed for Sb, with median value of 7 ± 2 ppm with contents up to 45 ± 15 ppm. Tin content is low with a median value of 1 ± 0.2 ppm. Lead is below 100 ppm for most of the studied sphalerite types except for type 1 sphalerite which shows higher content with a median value of 267 ± 37 ppm.

In type 2b, Fe content ranges from 1.3 to 5 wt% Fe but no systematic difference is observed between deposits or textures (Fig. 7). In Pale Bidau, a progressive zonation in color is observed (Fig. 4a and b), and high Fe contents are reported in dark brown sphalerite zones with values up to 5 wt% Fe. High Mn median values are reported for Anglas (151 ± 10 ppm), comparatively to Pale Bidau and Arre (24 ± 4 ppm and 18 ± 2 ppm, respectively). Conversely, low median Cd values are present in Anglas (970 ± 38 ppm) and higher median values for Pale Bidau and Arre (1500 ± 75 ppm and 1110 ± 43 ppm, respectively). No correlation between grain size or color and the contents in Fe, Mn, or Cd has been established. Cobalt content is homogeneous between the three textures (Fig. 7) with a median value of 143 ± 11 ppm. Low In content is measured in these sphalerite types reaching a maximum of 6.2 ppm (Fig. 7) and median value below 1 ppm. Indium content is slightly higher light coarse grains from Pale Bidau with a median value of 4.1 ± 0.2 ppm.

Gallium content is generally below 100 ppm in the sphalerite samples (Fig. 7) but exhibits relative large dispersion in concentrations between 0.3 and 156 ppm Ga which is not clearly related either to the type of grain or the deposit. Silver, Sn, Sb, and Pb contents are commonly below 100 ppm. Some Pb-(Sb-Sn-Ag) micrometric inclusions are recognized in LA-ICP-MS spectra (ESM 2) preferentially in recrystallized domains with Pb values reaching up to 9420 ppm.

Except for the presence of micro-inclusions, no clear difference between textures (Fig. 7) and deposits can be defined.

Germanium and Cu contents show generally large variations from 102 to 580 ppm for Ge and from 209 to 1265 ppm for Cu. These contents correlate with the type of texture (Fig. 4) and are detailed below.

In dark domains of coarser grains, Ge and Cu are typically high in the three deposits with median value of 290 ± 19 ppm and 610 ± 61 ppm, respectively (Fig. 7). In Pale Bidau, only few dark domain relicts ($n = 4$) are reported and analyzed with median values of 152 ± 20 ppm for Ge and 233 ± 45 ppm for Cu. Arre samples show the highest Ge and Cu contents with median contents of 433 ± 21 ppm and 1012 ± 75 ppm, respectively.

In light domains of coarse grains, Ge and Cu contents are lower with median values of 20 ± 2 and 60 ± 8 ppm, respectively (Fig. 7). Pale Bidau shows the lowest median contents, with 0.7 ± 0.1 ppm for Ge and 29 ± 4.5 ppm for Cu compared to Arre and Anglas which show median contents of respectively 38 ± 1 and 61 ± 3 ppm for Ge, and 102 ± 7 and 191 ± 13 ppm for Cu.

In recrystallized grains, Ge and Cu are systematically low like in light domains of coarse grains, with median contents of 4.3 ± 1 ppm and 49 ± 10 ppm, respectively (Fig. 7). In Pale Bidau, recrystallized grains may contain similar or larger enrichment in Ge and Cu than in light color domains of coarse grains, with respectively 4.1 ± 0.5 ppm and 102 ± 19 ppm.

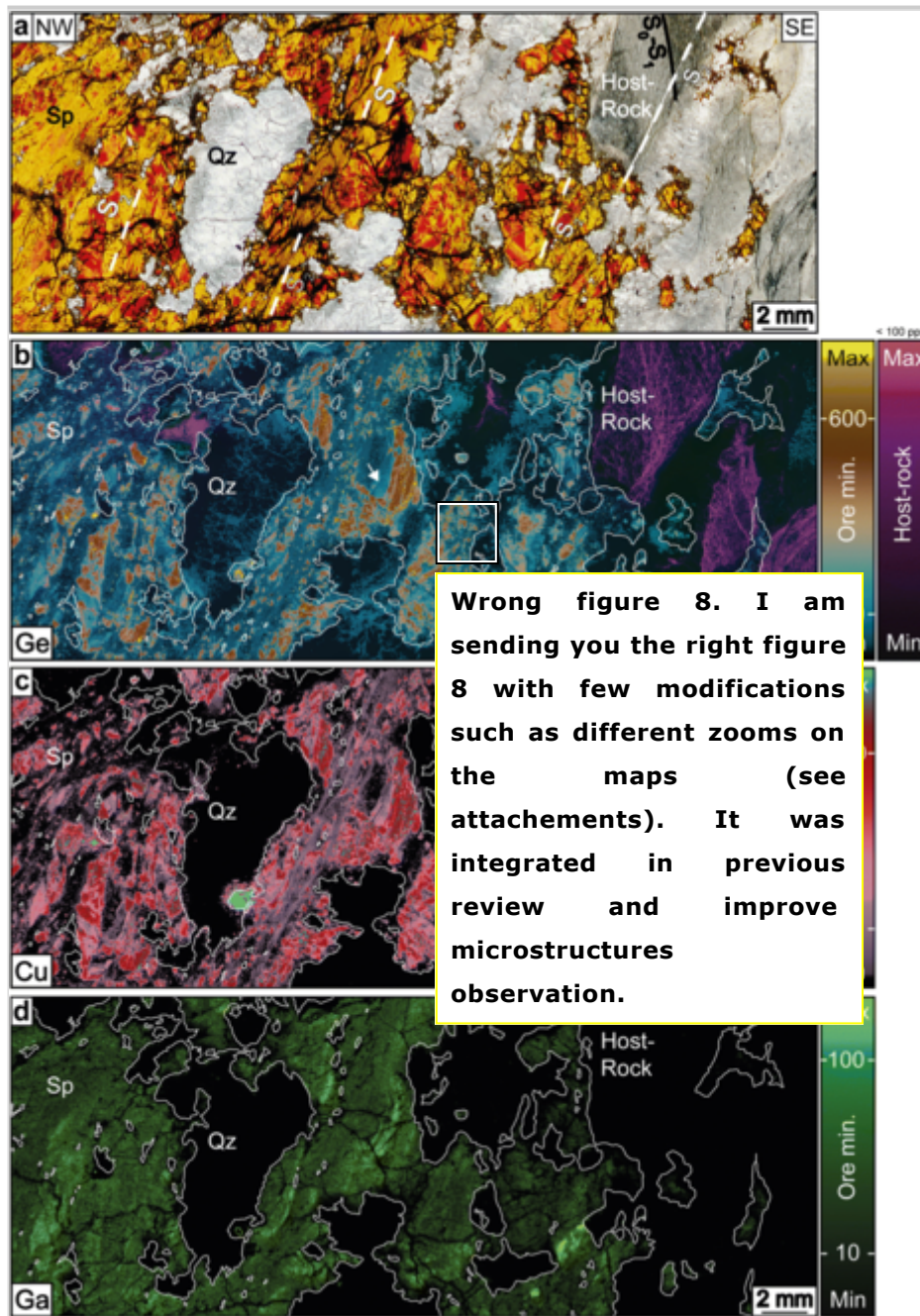
Spatial distribution of trace elements in sphalerite

Figure 8 shows Ge, Cu, and Ga spatial distribution obtained from LIBS mapping of Arre type 2b sphalerite. Sphalerite is zoned in color in transmitted-light (Fig. 8a), correlating with the concentration of these trace elements. Germanium and Cu contents are heterogeneous in sphalerite, with patchy zoning, and locally oscillatory zoning (Fig. 8) with numerous Ge- and/or Cu-bearing minerals (Fig. 8b and c), some of them with Fe correspond to briartite $\text{GeCu}_2(\text{Fe}, \text{Zn})\text{S}_4$ (ESM 2). Localized Ge-Cu minerals are preferentially found in sphalerite Ge-Cu-poor domains (ESM 2). Nonetheless, some of them occur in Ge and Cu-rich dark domains and are sub-parallel to S_2 cleavage (Fig. 8b and c).

Fig. 8

LIBS mapping on Arre type 2b (abbreviations: Qz: quartz; Sp: sphalerite). **a** Microphotograph (thick section, transmitted-light) of Arre sphalerite associated to quartz and calc-schist host-rock. **b** Ge map in sphalerite, quartz, and host-rock. Ge is also shown in purple color in the host rock (calc-schist) because it is measured

on a different spectral line due to Al interferences. White arrow indicates specific Ge zones. **c** Cu map in sphalerite, quartz, and host-rock. **d** Ga map in sphalerite, quartz, and host-rock



Mass-balance calculations are performed, based on LIBS mapping (see dataset in ESM 1). The bulk Ge concentration hosted in the Ge-rich minerals is 4.72 wt% Ge, based on 25 wt% Ge. Light and dark domains present 0.1 and 2.07 wt% Ge, respectively, considering Ge-poor and Ge-rich sphalerite with 20 and 400 ppm Ge, respectively. Germanium mass fraction is two times higher in Ge minerals than in sphalerite. The total Ge mass is equivalent to a sphalerite with 690 ppm Ge uniformly distributed in the structure without Ge minerals.

Gallium in sphalerite shows zoned distribution on LIBS maps. Gallium-rich areas are located in dark domains in transmitted light, correlating with relatively high Cu and Ge contents (Fig. 8d and ESM 2). Gallium-bearing mineral phases have not been detected. Other elements such as Fe and Cd show a homogeneous distribution in sphalerite (ESM 2).

Trace element distribution in quartz spatially associated with sphalerite is reported in Fig. 8. Several areas in quartz show enrichment in Ge, up to ~ 75 ppm (Fig. 8b). Copper and Ga have not been detected in quartz (Fig. 8c and d). In the host rock, a few Cu-bearing micrometer size grains are identified, and Ge is detected in structures parallel to S_0 - S_1 or S_2 (Fig. 8b) and correlate with the higher Al contents (ESM 2), which correspond to muscovite.

Discussion

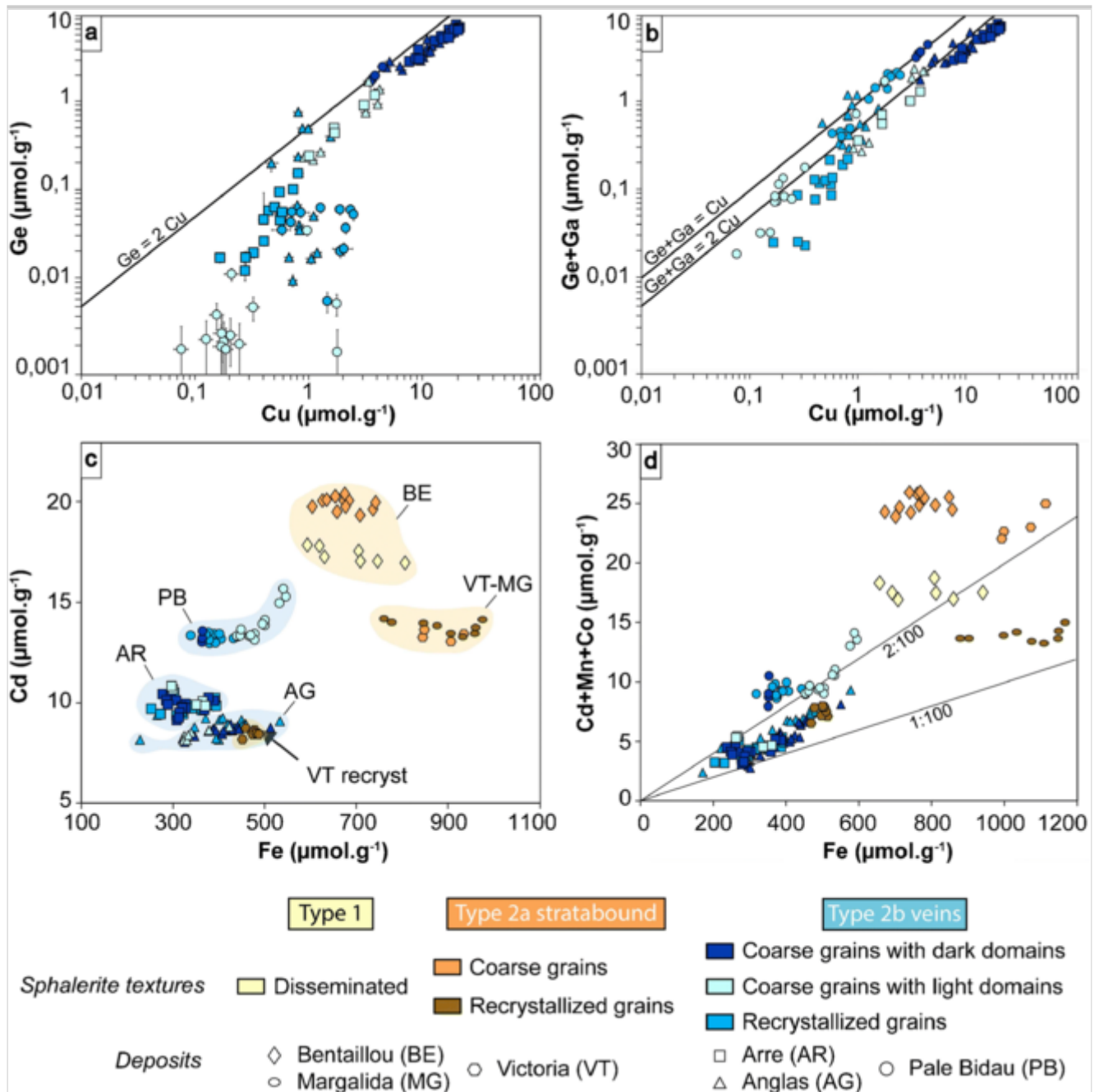
Substitution mechanisms of rare metals in sphalerite

The mechanism of Ge incorporation in sphalerite has been studied by Cook et al. (2009b) who deduced from the apparent lack of correlation with other trace elements that Ge could be present in a divalent form and substitute for Zn in the sphalerite structure ($Zn^{2+} \leftrightarrow Ge^{2+}$). Later, Cook et al. (2015) reported a XANES study performed on Tres Maria Ge-Fe rich acicular sphalerite, demonstrating Ge^{4+} in sphalerite and proposed substitution of Ge^{4+} and a vacancy for Zn^{2+} or Fe^{2+} (i.e., $2Zn^{2+} \leftrightarrow Ge^{4+} + []$). In Central and East Tennessee, Bonnet et al. (2017) showed Ge^{2+} and Ge^{4+} in the same sphalerite crystal, which was interpreted as due to a difference in S_2 and O_2 fugacities. Bauer et al. (2018) demonstrated a coupled substitution between Ge^{4+} and Ag^+ in low-temperature (186 ± 36 °C) Ge-rich sphalerite. Johan (1988) suggested a coupled substitution between tetravalent Ge and combination of monovalent and divalent Cu (i.e., $4Zn^{2+} \leftrightarrow 2Cu^+ + Cu^{2+} + Ge^{4+}$) on low-temperature Ge- and Cu-rich sphalerite from Saint-Salvy. Belissont et al. (2016) μ -XANES study on the same sphalerite confirmed the exclusive occurrence of Ge^{4+} in sphalerite, showing correlation with monovalent Cu^+ , supporting the hypothesis of a coupled substitution mechanism involving monovalent copper. This substitution $3Zn^{2+} \leftrightarrow 2Cu^+ + Ge^{4+}$ is consistent with the PAZ sphalerite 2Cu–Ge correlation in Fig. 9a. Coarse grains follow this substitution mechanism; however, the recrystallized grains as well as some of the coarse grains with light domains do not plot along the correlation line. For these two Ge-poor domains, such a deviation to the regression line may be explained by the incorporation of Cu coupled to an additional substitution involving Ga (Fig. 9b). Gallium in sphalerite is considered to be trivalent (Cook et al. 2009b; George et al. 2016; Wei et al.

2018) and its incorporation occurs following the coupled substitution $2\text{Zn}^{2+} \leftrightarrow \text{Cu}^+ + \text{Ga}^{3+}$.

Fig. 9

Content of elements for type 1, 2a, and 2b sphalerite. In coarse grains within dark domains, analyses are close to the Ge–2Cu line. **a** Ge vs Cu contents. Recrystallized grains and light domains in the coarse grains do not lie on the correlation line. Pale Bidau coarse grains within light domains contain very low Ge contents. **b** Ge + Ga vs Cu contents. All the points lie closely to the substitution $\text{Ge} + \text{Ga} = 1\text{Cu}$ or 2Cu depending on the dominant element in the sphalerite lattice (Ge or Ga). **c** Cd vs Fe contents. Note that each deposit forms a cluster. Recrystallized grain concentrations from Victoria deposit are close to Anglas deposit. **d** Cd + Mn + Co vs Fe contents. Note the correlated enrichment between Cd + Mn + Co and Fe contents. Recrystallized grains compositions from Victoria deposit are close to Anglas deposit



Divalent cations such as Cd^{2+} , Mn^{2+} , Co^{2+} , or Fe^{2+} are incorporated by direct substitution with Zn^{2+} ($\text{X}^{2+} \leftrightarrow \text{Zn}^{2+}$, Cook et al. 2009b; George et al. 2016). No clear correlation is observed between Cd^{2+} and Fe^{2+} (Fig. 9c), but the Cd-Fe values are mainly varying according to the deposit, indicating poor mobility during vein recrystallization. In Fig. 9d, Fe is significantly correlated with Cd+Mn+Co at low values, which attests for their coupled incorporation in sphalerite.

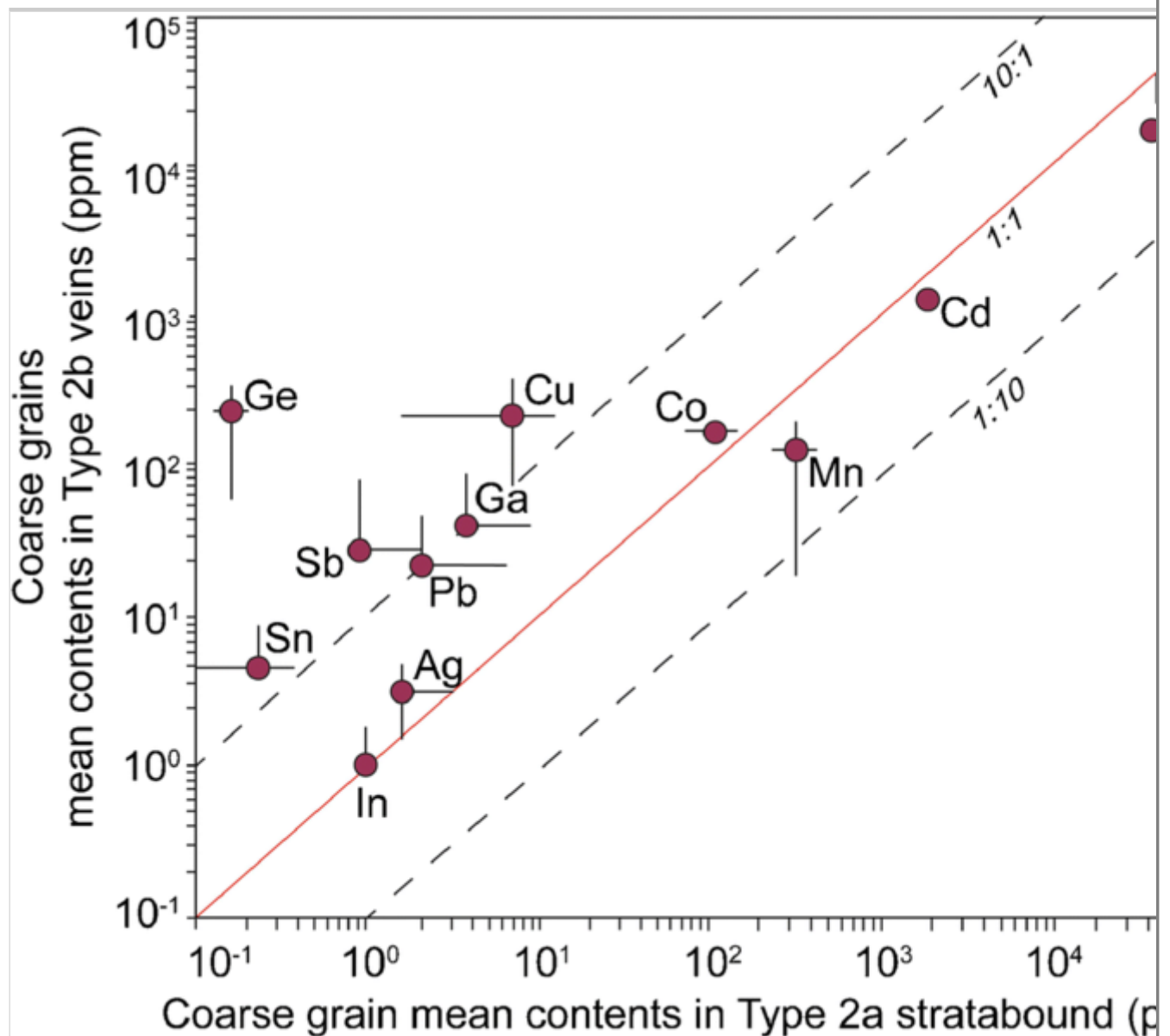
Relationship between sphalerite texture, chemical composition, and formation temperature

Crystallization temperature of vein assemblages is difficult to assess, but we use relative field chronology to place vein formation in the regional

tectonometamorphic framework. M_1 peak is estimated at 580 °C and 0.55 GPa, and M_2 peak at 525 °C and 0.2 GPa (Mezger and Passchier 2003; Mezger et al. 2004). The three sphalerite mineralization types show significant differences in trace element signatures. Types 1 and 2a have low Ge content (< 0.5 ppm), as well as Cu, Ga, and Ag, Sb, Sn, Pb but higher Fe, Mn, and Cd contents (Fig. 10). Type 1 disseminated mineralization from Bentaillou is considered pre-metamorphic and has been affected by Variscan M_1 regional and M_2 contact metamorphism (Cugerone et al. 2018b).

Fig. 10

Trace element comparison of coarse sphalerite grains between type 2b and type 2a crystals



Type 2a sphalerite from Bentaillou, Victoria, and Margalida is syn- M_1 and prior to D_2 associated with F_2 folds (Fig. 3) and M_2 metamorphism. During

metamorphism, sphalerite can incorporate Fe, Mn, and Cd and in a lesser extent Pb, Bi, Ag, Sn, and Sb (Lockington et al. 2014) during static recrystallization. Accordingly, type 2a sphalerite that was statically (coarse-size fraction) and subsequently dynamically recrystallized (small-size fraction) in Victoria deposit shows respectively high and low Fe, Cd, and Mn contents (Figs. 6 and 8c, d). The geothermometer based on Ga-Ge-In-Mn-Fe concentrations in sphalerite lattice (GGIMF, Frenzel et al. 2016) was applied for type 1 and 2a sphalerite (see dataset in ESM 1) and yields temperatures below 150 °C. Sphalerite underwent static recrystallization at temperatures, likely above 400 °C, and in some areas subsequent dynamic recrystallization, which affect the reliability of the GGIMF geothermometer (Frenzel et al. 2016), such that, this temperature is not that of mineralization or deformation.

The chemical composition of type 2b sphalerite from the Anglas and Arre deposits is heterogeneous. Germanium, Cu, and locally Ga are enriched in coarse grains with dark domains (Fig. 8) but depleted in recrystallized grains and coarse crystals with light domains (Cugerone et al. 2020). At Pale Bidau, no strong chemical zonation is observed in sphalerite, except some color bands that highlight contrasts in Fe contents (Cugerone et al. 2018a). However, Ge-poor coarse crystals can be found (Fig. 4b), the latter being interpreted as inherited Ge-poor domains.

Type 2b mineralization has low Cd and Fe contents. Variations in Cd content between the Arre-Anglas and Pale Bidau deposits might be linked to differences in the fluid source or in the bulk host rock composition. The Arre and Anglas deposits are hosted by similar Devonian sequences in the same mining district, contrary to Pale Bidau which is hosted by Late-Ordovician calc-schists (Cugerone et al. 2018b, Fig. 1). Cadmium content in type 2b mineralization is generally not affected by recrystallization. Nonetheless, type 2a recrystallized and coarse sphalerite grains from the Victoria deposit present differences in Cd concentrations, as well as in Fe, Mn, and Co. Recrystallized grains from Victoria have similar low Cd-Fe concentrations to type 2b sphalerite from the Anglas deposit. A likely hypothesis is that type 2b mineralization resulted from remobilization of early type 2a mineralization in D₂ structures, such as Victoria F₂ fold hinge (Fig. 3). However, this hypothesis is restricted by the lack of Ge minerals in recrystallized sphalerite and by the relatively low Ge, Cu, or Ga contents in the type 2a mineralization. Late Ge-Cu(-Ga)-rich fluids circulating in S₂ cleavage plane during type 2b mineralizing event may have been the main Ge-carrier.

If type 2b primary sphalerite had the same chemical composition as coarse grains, the estimated temperature, using GGIMF, is about 250 °C, with large

variations of ± 50 °C due to chemical heterogeneity between dark and light domains. This geothermometer may be applied in dark domains of the coarse grains, if we consider no change in composition after the primary mineralizing stage. However, in light domains, composed of recrystallized grains and some part of the coarse grains, the temperature recorded is inconsistent. Deformation and recrystallization of the sphalerite lattice have contributed to the redistribution of the elements used in GGIMF thermometry. Germanium-rich veins are commonly formed at low temperatures, below 200–250 °C (Munoz et al. 1994; Höll et al. 2007; Belissont et al. 2014; Frenzel et al. 2016; Bauer et al. 2018). There is no fluid inclusion study yet for the PAZ mineralization to compare with the GGIMF. Johnson et al. (1996) have investigated fluid inclusions in the Cierco deposit where Pb-Zn veins similar to the PAZ type 2b veins appear (Fig. 1b). At Cierco, some Ge-minerals have been identified in recrystallized sphalerite hosted in Late-Variscan granodiorite. This likely indicates that at least a part of the mineralization, belongs to type 2b (Johnson et al. 1996). Primary or pseudo-secondary fluid inclusion microthermometry in quartz and sphalerite yield temperature between 150° and 200 °C with salinities between 3 and 29 wt% NaCl equivalent. Pressure is assumed to be negligible (Johnson et al. 1996). No clear petrographic relationship or evidences between fluid inclusions and host-minerals is described and their primary or pseudo-secondary origins are questionable in a largely deformed environment .

(Castroviejo Bolibar & Serrano, 1983).

In our samples, pressure-temperature conditions of deformation events, which are syn- or post-mineralization, are difficult to assess. Experimental studies on carboirite bracket its stability field between 340 and 600 °C and 0.75 to 2 MPa whereas brunogeierite is reported above 510 °C at 2 MPa (Julliot et al. 1987). Quartz crystals appear only slightly deformed, preserving original cockade textures and no alteration halo is observed along the vein contacts. Partial recrystallization of the Pyrenean sphalerite is localized in bands associated to a pronounced cleavage, parallel to the S_2 cleavage of the host rock (Figs. 4 and 8). Such a partial recrystallization might occur at temperatures below 400 °C and low pressure in comparison with experimental studies on sphalerite that evidence dynamic recrystallization of sphalerite at low-metamorphic grade (Clark and Kelly 1973; Siemes and Borges 1979; Couderc et al. 1985; Cox 1987). Recrystallization of sphalerite at higher-metamorphic grade will result loss of parent grains in favor of recrystallized grains.

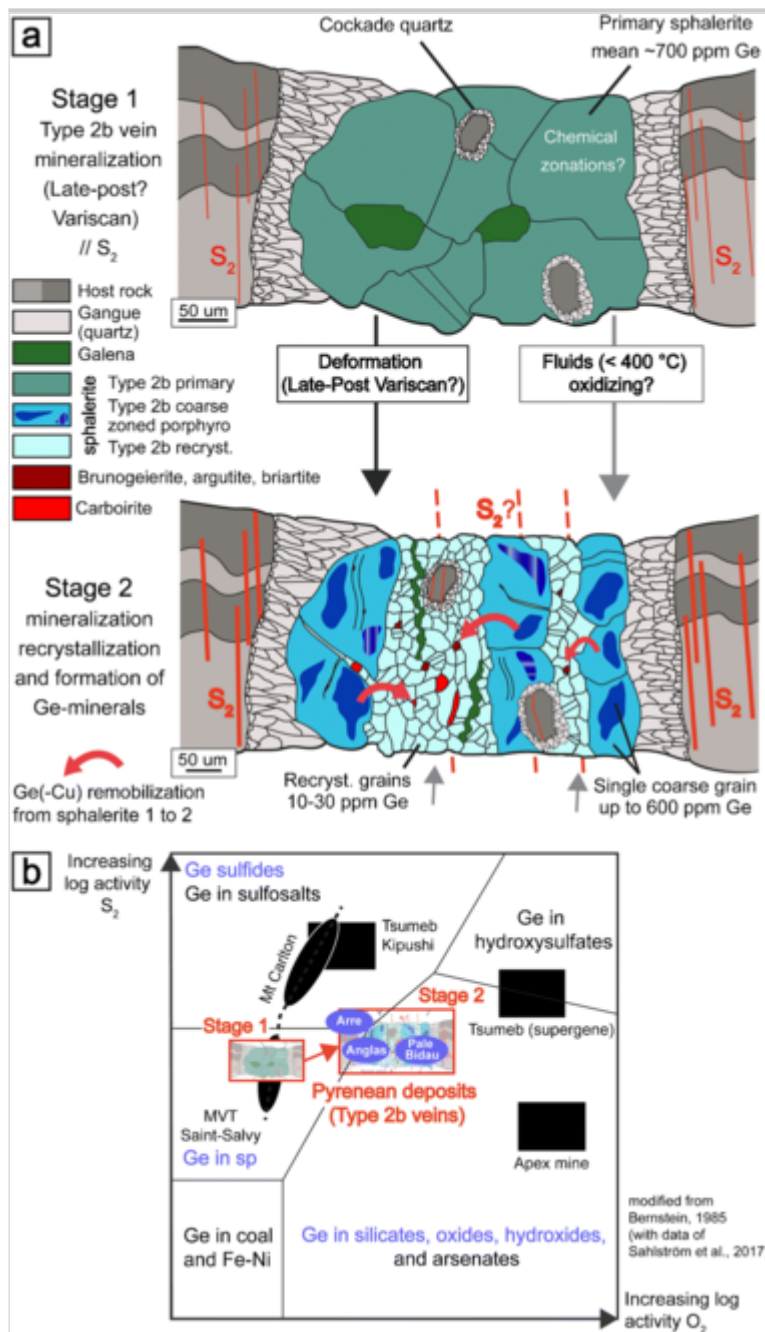
Mechanisms of formation of accessory minerals

Germanium minerals are exclusively located in type 2b veins which have been affected by subgrain rotation recrystallization or in close association with weak

structures such as twin boundaries (Fig. 8b; Cugerone et al. 2020). Figure 11a shows a genetic model of their formation. Stage 1 represents the primary type 2b mineralization hosted in an undeformed vein and Ge is in the sphalerite lattice. Stage 2 is characterized by dynamic recrystallization of sphalerite related to subgrain rotation mechanism (Cugerone et al. 2020) and the formation of Ge-minerals. Ge-minerals are not included in sphalerite and are commonly located at sphalerite triple junctions (Fig. 5d and f). They rim the grain boundaries of recrystallized sphalerite, which attests of their late formation.

Fig. 11

a Two stage genetic model of the formation of Ge-minerals and sphalerite textures and chemical composition in type 2b Pb-Zn mineralization. Stage 1 represents the mineralization before D_2/M_2 Variscan deformation. Stage 2 is the mineralization after deformation. **b** Behavior of Ge in different geologic environments and minerals according to fO_2 and fS_2 for the two type 2b stage described in **a**. Experimental data were acquired between 27 and 327 °C (300 to 600 K) and 0.1 MPa (modified from Bernstein 1985 with values of Sahlström et al. 2017). Stage 2 is [plots](#) "shown" instead of "plots" in three different fields according to the deposit: sulfide, sphalerite, and oxide fields. The Arre deposit is restricted to the "Ge-sulfides" field due to abundance of briartite and rare carboirite and brunogeierite. The Anglas and Pale Bidau deposits contain both carboirite and brunogeierite but briartite is rare. Germanium in sphalerite lattice occurs quasi exclusively in Arre and Anglas. Ge-hosts in blue represent the Ge-carrier in the PAZ Pb-Zn deposits



Occurrence of intragranular oscillatory zonations (Plümper et al. 2012) may inform on diffusion mechanisms (Fig. 8 and ESM 2) within sphalerite coarse grains in dark to light domains. Intragranular diffusion is comprised of different mechanisms such as volume, high diffusivity pathway, or dislocation-impurity pair diffusion (Klinger and Rabkin 1999; Reddy et al. 2007; Plümper et al. 2012; Vukmanovic et al. 2014). In addition, hydrothermal fluids might have percolated and extract Ge, Cu, and Ga from the sphalerite lattice along grain boundaries, and twin cleavage planes which constituted nucleation sites as Ge(-Cu) minerals are abundant in such locations (Fig. 5). In hydrothermal fluids, Ge is transported as a $Ge(OH)_4$ complex, and its solubility increases with temperature (up to 400 °C; Pokrovski and Schott 1998; Pokrovski et al. 2005). In the Arre deposit, direct correlation between Ge and Cu in sphalerite lattice and in accessory minerals (briartite; Fig. 8b and c) attests to the similar behavior of these two

elements during remobilization. It could be linked to similar ionic radius (Shannon 1976) or specific conditions enhancing the extraction and coupled incorporation in accessory phases. In the Pale Bidau and Anglas deposits (Fig. 4a, b and e, f), Ge-minerals such as carboirite and brunogeierite do not contain high Cu contents which may indicate possible differences in Ge and Cu behavior. Gallium is only found in coarse grains (< 100 ppm Ga), mostly correlated to Ge- and Cu-rich areas in the sphalerite lattice (Fig. 8), but no Ga enrichment occurs in Ga-bearing phases which may be due to loss of this metal or to low primary content in sphalerite (Fig. 8). No impact of recrystallization on Cd concentrations is detected in sphalerite (ESM 2). Cadmium is mainly transported as chloride water complexes in hydrothermal fluids ($20 \leq T \leq 450$ °C; Bazarkina et al. 2010) whereas hydroxyl complexes generally transport Ge ($[\text{GeOH}]_4$); Pokrovski and Schott 1998) and more rarely Cu ($[\text{CuOH}]$; Hack and Mavrogenes 2006) at low pressure (< 500 MPa). Hydroxyl complexes might be the main rare metal-bearing complexes in hydrothermal fluid during the remobilization stage.

Fields of stability of Ge in different minerals according to $f\text{O}_2$ and $f\text{S}_2$ indicate potential $f\text{O}_2$ increase during formation of Ge-minerals during the stage 2 (Fig. 11b). Increasing of $f\text{O}_2$ may enhance the release of Ge from sphalerite lattice by circulation of low-temperature fluids which significantly change and diversify the Ge-mineral paragenesis (silicates, oxides, hydroxides, sulfide). It is important to note that hydrothermal fluids responsible for Ge remobilization during deformation do not need to be rich in Ge, if we consider a primary sphalerite with uniform ~ 700 ppm Ge content (Fig. 11a and ESM 1). These arguments allow to demonstrate that a primary Ge-rich sphalerite (and other sulfides) impacted by low-grade deformation below 400 °C with significant increase in $f\text{O}_2$ (Fig. 11b) are potential indicators of Ge-mineral rich deposit.

Comparison with world-class Ge-rich deposits

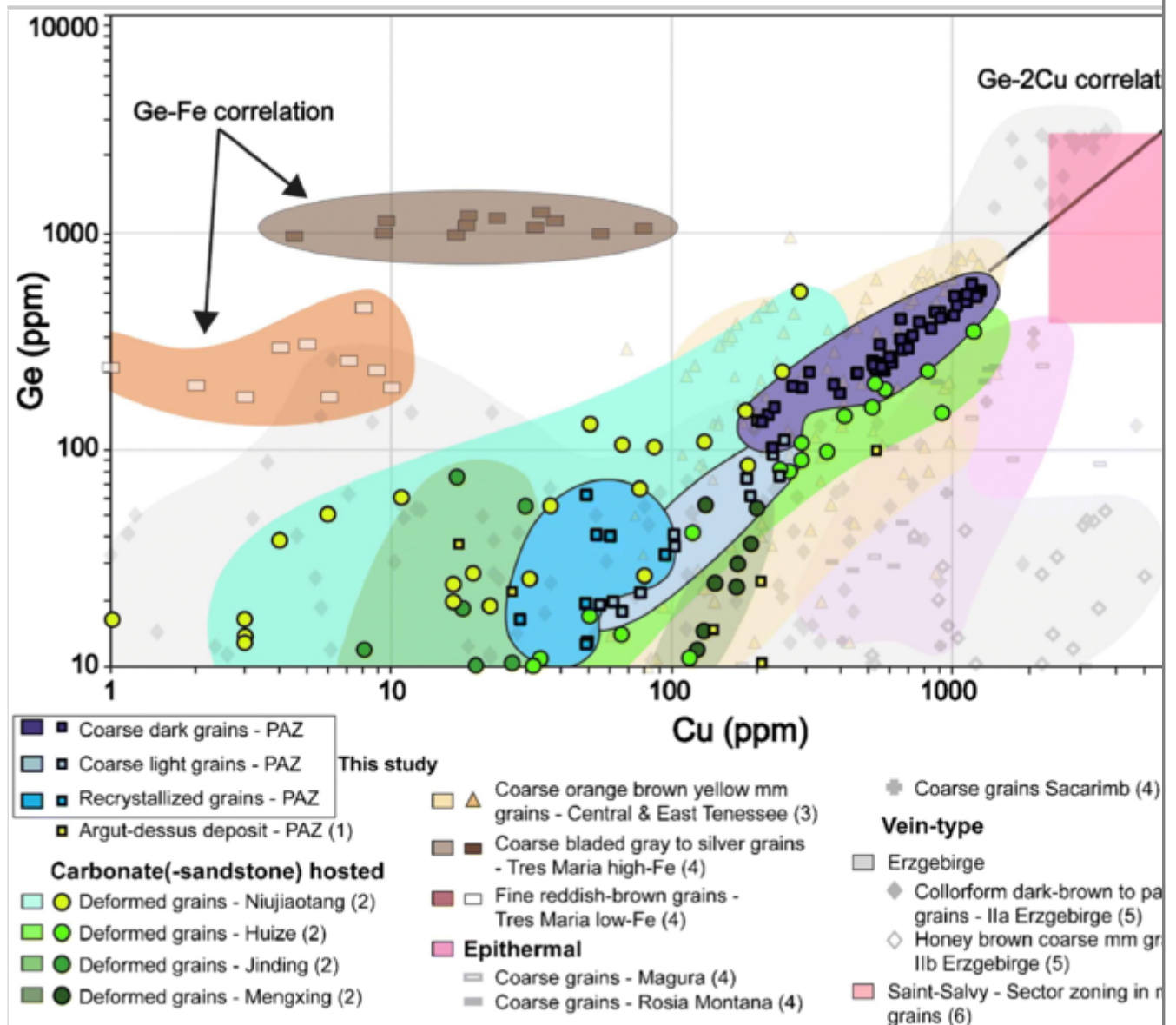
Type 2b sphalerite vein mineralization from the PAZ present chemical and textural similarities with world-class Pb-Zn(-Ge) districts. In many SHMS, VMS, or other Pb-Zn(-Cu) deposits, metamorphism and deformation may have reworked the mineralization (Bodon 1998; Large et al. 2005; Huston et al. 2006; Wilkinson 2013; Vikentyev et al. 2016) as shown by partly dynamically recrystallized sphalerite at the world class George Fisher (Chapman 2004; Murphy 2004) or in the Currawong deposits (Bodon and Valenta 1995). However, too few chemical analyses of rare metals have been performed in these deposits. As an example, Fig. 12 reports a compilation of Ge and Cu contents in sphalerite analyzed in Pb-Zn(-Cu) deposits worldwide. These deposits are mostly related to low-temperature hydrothermal fluids (~ 100 – 250 °C) with no-

or only low-grade deformation. Numerous studies on Pb-Zn(-Cu) deposits deformed or metamorphosed at higher grades ($> 400\text{ }^{\circ}\text{C}$) do not report significant rare metals contents in sphalerite or in accessory Ge-minerals and may be related, in some cases, to insufficient textural and chemical investigation. Nonetheless, in all Pb-Zn deposits affected by high-grade metamorphism, Ge was lost from sphalerite during high-grade metamorphic processes ($> 400\text{ }^{\circ}\text{C}$) and recrystallization has potentially concentrated Ge in accessory minerals. This assumption is likely for the granulite facies Broken Hill deposit (Spry et al. 2008; George et al. 2016) where Ge is not reported in sphalerite, while the Ga and In contents are low, suggesting that these rocks should be revisited for accessory minerals rich in rare metals.

Fig. 12

Germanium vs copper contents comparison between Pyrenean sphalerite (including Argut-dessus deposit; Cugerone et al. 2018a) and others sphalerite in the world. A lower Ge limit of 10 ppm is set to compare Ge-rich sphalerite. Germanium and copper measurements generally follow the line $\text{Ge} = 2\text{Cu}$ when Ge is enriched in the sphalerite lattice, with the exception of the Tres Maria zinc sulfide. [1—Niujaotang, Huize, Jinding, and Mengxing deposits: 2—Ye et al. \(2011\);](#) missing one reference:

1- Argut-dessus: Cugerone et al. (2018a); 2-Niujaotang, Huize, Jinding, and Mengxing deposits: Ye et al. (2011); ... 3—Central and East Tennessee deposits: Bonnet (2014); 4—Tres Maria, Magura, Rosia Montana, Sacarimb deposit: Cook et al. (2009a, 2009b); 5—Erzgebirge deposits: Bauer et al. (2018); 6—Saint-Salvy deposit: Belissont et al. (2014)



Examples of Ge-rich sphalerite in the Saint-Salvy deposit, Montagne Noire (France), in the Erzgebirge district (Germany), and in MVT deposits from the Central and East Tennessee indicate that Ge is in bands within a single crystal (Bonnet 2014; Bauer et al. 2018) or in sector zones (Belissont et al. 2014) and may reach up to ~ 3000 ppm Ge (Fig. 12) with no Ge minerals reported.

In Ge-rich sphalerite, a correlation between Ge and Cu is observed except with the Tres Maria deposit where Ge is mainly correlated to Fe (Fig. 12). Wurtzite, a non-cubic zinc sulfide, is inferred in the zinc ore at Tres Maria (type I mineralization; Cook et al. 2009b, 2015; Saini-Eidukat et al. 2009) due to an acicular habit, similar to the wurtzite observed in the Kokanee range by Beaudoin (2000).

Rare elements (Ge, Ga, In, Cd) are reported in deformed sulfide deposits such as Barrigão, a remobilized Cu-rich VHMS deposit. Germanium-rich chalcopyrite with heterogeneous contents and Sn-Ge-rich phases (Reiser et al. 2011) are

probably a result of Ge remobilization during deformation (Belissont et al. 2019). In China, Pb-Zn deposits, considered to be deformed MVT deposits, contain abundant deformed sphalerite mineralization as in Huize (Han et al. 2006), Niujiaotang (Ye and Tiegeng 1999; Ye et al. 2012), Mengxing (Ye et al. 2011), Jinding (Xue et al. 2007) and Lehong (Wei et al. 2019). Germanium and Cu contents from these deposits are plotted in Fig. 12 and show that the chemical composition of these deposits is similar to that of the PAZ deposits, but with a wider dispersion along the Ge-Cu arrow. Wei et al. (2019), focusing on the carbonate-hosted Lehong deposit, described dark brown Ge-rich sphalerite and light-brown Ge-poor sphalerite with Ge content similar to Pyrenean vein mineralization with up to 536 ppm and 118 ppm in dark and light-brown domains, respectively. However, no detail on the texture of these sphalerite grains is provided, and Ge-minerals are not reported. Another example of deformed sphalerite mineralization is reported by Monteiro et al. (2006) in the carbonate-hosted Fagundes Pb-Zn deposit, where large variations in Ge (up to 2390 ppm Ge) were measured. Based on similarities with our observations, this heterogeneity in Ge content may be related to differences in sphalerite texture such as type 2b sphalerite in the PAZ.

Germanium minerals were reported in the Kipushi-type deposits (Emslie 1960; Francotte et al. 1965; Ottemann and Nuber 1972). Belissont (2016) describes highly variable Ge contents, from 0.2 to 5930 ppm, in sphalerite from the Kipushi mine that presents evidence of dynamic recrystallization (Hughes 1987). At the Black Angel deposit, Greenland (Horn et al. 2018), sphalerite is depleted in Ge and Cu, and the occurrence of briartite is reported. In the Eastern-Alpine base-metal sulfide ores, a LA-ICP-MS study indicates Ge-rich mineralization in carbonate-hosted Pb-Zn deposits (Melcher and Onuk 2019). The analyses reveal that the Ge content in sphalerite is highly variable (from < 1 up to 3700 ppm). Moreover, renierite $(\text{Cu,Zn})_{11}(\text{Ge,As})_2\text{Fe}_4\text{S}_{16}$ is reported as inclusions in bornite from one of these deposits.

Conclusions

Type 2a stratabound mineralization in the PAZ was affected by static recrystallization and local dynamic recrystallization during M_2 metamorphism. In such mineralization, sphalerite is largely depleted in Ge, Cu, and Ga, but generally enriched in Cd. However, Cd content has been found to be variable depending on the type of deposit and the texture, with substantial depletion during dynamic recrystallization.

Type 2b mineralization, interpreted as dynamically recrystallized Pb-Zn vein mineralization, shows chemical heterogeneity in sphalerite, particularly in terms

of Ge and Cu contents, which are related to deformation at relatively low-temperature ($< 400\text{ }^{\circ}\text{C}$) associated with a possible increase in $f\text{O}_2$. Gallium is depleted in the recrystallized fraction and recrystallization does not have significant impact on Cd concentrations. The interplay between diffusion and dissolution processes in sphalerite may account for large variations in Ge and Cu contents and the precipitation of Ge minerals.

Textural and chemical heterogeneity is frequent in Pb-Zn deposits around the world. Understanding the coupling between microstructures and chemistry has major implications on evaluating rare element potential of deposits. In this study, we show that exploration for rare and critical metals (Ge, Ga, In) must integrate micro-textural and in situ chemical analyses of sulfides. In cases of dynamic recrystallization of sphalerite, we show in situ analysis by LA-ICP-MS is not sufficient to provide a good screening of critical metals. In such case, these elements will be accumulated in discrete solid phases that can be found using chemical maps. These small minerals can be often responsible for the high dispersion of bulk and in situ chemical data. Dynamic recrystallization of sphalerite appears to be widespread in all orogenic fields. The recognition of these textures is essential in a first stage to locate enrichment of rare metals in specific mineral phases. Numerous deformed Pb-Zn(-Cu) such as in SEDEX, MVTs, or Kipushi-type deposits should be further explored for their contents of rare metal.

Publisher's note

Springer Nature remains neutral with regard to jurisdictional claims in published maps and institutional affiliations.

Acknowledgments

Bénédicte Cenko-Tok acknowledges funding from the European Union's Horizon 2020 Research and Innovation Program under grant agreement no. 793978. The authors gratefully acknowledge Christophe Nevado and Doriane Delmas for the exceptional thin sections preparation, Olivier Bruguier for his involvement in LA-ICP-MS analyses, and Fabrice Barou for the acquisition of the EBSD analyses. The authors are thankful to Prof. Hans Albert Gilg and Prof. Georges Beaudoin for the editorial handling and to Prof. Steven Reddy and Dr. Max Frenzel for their highly constructive comments.

Funding information

This study was funded through the French national program "Référentiel Géologique de France" (RGF-Pyrénées) of the French Geological Survey

(Bureau de Recherches Géologiques et Minières; BRGM) and through the INSU-CNRS Tellus CESSUR program.

Electronic supplementary material

ESM 1

Chemical datasets. **Table S1** In-situ LA-ICP-MS dataset of the Type 1, Type 2a and Type 2b mineralizations. **Table S2** Mass balance calculation in Ge-rich sphalerite from the Arre deposit. **Table S3** GGIMF geothermometer calculation of the in-situ LA-ICP-MS data based on the equation from Frenzel et al. (2016) (XLSX 105 kb)

ESM 2

Additional figure and LIBS maps. **Fig. S1** Time-integrated representative LA-ICP-MS spectra of sphalerite. Ge spectra is represented in red color. i Spectra in coarse grains with dark domains (see sample description below). Note the smooth profile for Ge (401 ppm) and most of the element (except for Sb) which contain micrometric minerals (Anglas sphalerite, cc_37). ii Spectra in coarse grain with light domains (see sample description below). Note the smooth and lower signal for Ge (76 ppm) and a small Sb mineral at the beginning of the signal acquisition (~180 sec.) (Anglas sphalerite, cc_25). iii Spectra in recrystallized grains (see sample description below) with very low Ge content (0.8 ppm) and relatively smooth signal for the other elements (Anglas sphalerite, cc_34). iv Spectra in recrystallized grain with the presence of Fe-Ge-Cu-rich phases. The signal is divided in particular rich-phases field (1) and sphalerite field (2) (Anglas sphalerite, cc_10). v Spectra in recrystallized grain with occurrence of high Pb content (9420 ppm) in two micro-phases (Pale Bidau sphalerite, ce_18). **Fig. S2** LIBS mapping on Arre Type 2b ore mineralization. The analyzed area corresponds to the Fig. 8. i Zn map. ii Si map. iii Fe map. iv Cd map. v Al map. vi Mg map. vii Ti map. **Fig. S3** Transmitted-light microphotograph of the ore mineralization area analyzed with LIBS. **Fig. S4** Germanium high-resolution LIBS map. **Fig. S5** Copper high resolution LIBS map. **Fig. S6** Gallium high resolution LIBS map (PDF 3453 kb)

References

AQ3

Bauer ME, Burisch M, Ostendorf J, Krause J, Frenzel M, Seifert T, Gutzmer J (2018) Trace element geochemistry of sphalerite in contrasting hydrothermal fluid systems of the Freiberg district, Germany: insights from LA-ICP-MS analysis, near-infrared light microthermometry of sphalerite-hosted fluid inclusions, and sulfur isotope geochemi. *Mineral Deposits* 54:237–262

Bazarkina EF, Pokrovski GS, Zotov AV, Hazemann JL (2010) Structure and stability of cadmium chloride complexes in hydrothermal fluids. *Chem Geol* 276:1–17. <https://doi.org/10.1016/j.chemgeo.2010.03.006>

Beaudoin G (2000) Acicular sphalerite enriched in Ag, Sb, and Cu embedded within color-banded sphalerite from the Kokanee Range, British Columbia, Canada. *Can Mineral* 38:1387–1398. <https://doi.org/10.2113/gscanmin.38.6.1387>

Belissant R (2016) Germanium and related elements in sulphide minerals: crystal chemistry, incorporation and isotope fractionation. Ph D Thesis Univ Lorraine-Georessources-CRPG p210

Belissant R, Boiron M-C, Luais B, Cathelineau M (2014) LA-ICP-MS analyses of minor and trace elements and bulk Ge isotopes in zoned Ge-rich sphalerites from the Noailhac - Saint-Salvy deposit (France): insights into incorporation mechanisms and ore deposition processes. *Geochim Cosmochim Acta* 126:518–540. <https://doi.org/10.1016/j.gca.2013.10.052>

Belissant R, Munoz M, Boiron M-C, Luais B, Mathon O (2016) Distribution and oxidation state of Ge, Cu and Fe in sphalerite by μ -XRF and K-edge μ -XANES: insights into Ge incorporation, partitioning and isotopic fractionation. *Geochim Cosmochim Acta* 177:298–314. <https://doi.org/10.1016/j.gca.2016.01.001>

Belissant R, Munoz M, Boiron M-C, Luais B, Mathon O (2019) Germanium crystal chemistry in Cu-bearing sulfides from micro-XRF mapping and micro-XANES spectroscopy. *Minerals* 9:1–12. <https://doi.org/10.3390/min9040227>

Bernstein LR (1985) Germanium geochemistry and mineralogy. *Geochim Cosmochim Acta* 49:2409–2422. [https://doi.org/10.1016/0016-7037\(85\)90241-8](https://doi.org/10.1016/0016-7037(85)90241-8)

Bernstein LR, Cox DP (1986) Geology and sulfide mineralogy of the Number One Orebody, Ruby Creek copper deposit, Alaska. *Geology* 81:1675–1689

Bodon SB (1998) Paragenetic relationships and their implications for ore genesis at the Cannington. *Econ Geol* 93:1463–1488

Bodon SB, Valenta RK (1995) Primary and tectonic features of the Currawong Zn-Cu-Pb(-Au) massive sulfide deposit, Benambra, Victoria: implications for ore genesis. *Econ Geol* 90:1694–1721

Bonnet J (2014) Distribution et contrôle cristallographique des éléments Ge, Ga et Cd dans les sphalérites des gisements de type Mississippi Valley dans les districts de Central et East Tennessee, USA Ph D Thesis Univ Lorraine-Georesources 204

Bonnet J, Cauzid J, Testemale D, Kieffer I, Proux O, Lecomte A, Bailly L (2017) Characterization of germanium speciation in sphalerite (ZnS) from Central and Eastern Tennessee, USA, by X-ray absorption spectroscopy. *Minerals* 7:1–16. <https://doi.org/10.3390/min7050079>

BRGM (1984) Les gisements de Pb-Zn français (situation en 1977). BRGM Intern Rep:1–278

Cáceres JO, Pelascini F, Motto-Ros V, Moncayo S, Trichard F, Panczer G, Marín-Roldán A, Cruz JA, Coronado I, Martín-Chivelet J (2017) Megapixel multi-elemental imaging by laser-induced breakdown spectroscopy, a technology with considerable potential for paleoclimate studies. *Sci Rep* 7:1–11. <https://doi.org/10.1038/s41598-017-05437-3>

Carreras J, Druguet E (2014) Framing the tectonic regime of the NE Iberian Variscan segment. Schulmann, K, al, eds, *Variscan Orogeny Extent, Timescale Form Eur Crust Geol Soc London, Spec Publ* 405:249–264. <https://doi.org/10.1144/SP405.7>

Carvalho JRS, Relvas JMRS, Pinto AMM, Frenzel M, Krause J, Gutzmer J, Pacheco N, Fonseca R, Santos S, Caetano P, Reis T, Gonçalves M (2018) Indium and selenium distribution in the Neves-Corvo deposit, Iberian Pyrite Belt, Portugal. *Mineral Mag* 82:S5–S41. <https://doi.org/10.1180/minmag.2017.081.079>

Castroviejo Bolibar R, Serrano FM (1983) Estructura y metalogenia del campo filoniano de Cierco (Pb-Zn-Ag), en el Pirineo de Lérida. *Bol Geol Min* 1983:291–320

- Cerny I, Schroll E (1995) Heimische Vorräte an Spezialmetallen (Ga, In, Tl, Ge, Se, Te und Cd) in Blei-Zink- und anderen Erzen. Arch für Lagerstättenforsch der Geol Bundesanstalt 18:5–33
- Chapman LH (2004) Geology and mineralization styles of the George Fisher Zn-Pb-Ag deposit, Mount Isa, Australia. Econ Geol 99:233–255. <https://doi.org/10.2113/gsecongeo.40.7.431>
- Clark BR, Kelly WC (1973) Sulfide deformation studies; I, experimental deformation of pyrrhotite and sphalerite to 2,000 bars and 500 degrees C. Econ Geol 68:332–352. <https://doi.org/10.2113/gsecongeo.68.3.332>
- Cochelin B, Lemirre B, Denèle Y, De Saint BM, Lahfid A, Duchêne S (2017) Structural inheritance in the Central Pyrenees: the Variscan to Alpine tectonometamorphic evolution of the Axial Zone. J Geol Soc Lond 175:336–351. <https://doi.org/10.1144/jgs2017-066>
- Cook NJ, Ciobanu CL, Mao J (2009a) Textural control on gold distribution in As-free pyrite from the Dongping, Huangtuliang and Hougou gold deposits, North China Craton. Chem Geol 264:101–121. <https://doi.org/10.1016/j.chemgeo.2009.02.020>
- Cook NJ, Ciobanu CL, Pring A, Skinner W, Shimizu M, Danyushevsky L, Saini-Eidukat B, Melcher F (2009b) Trace and minor elements in sphalerite: a LA-ICPMS study. Geochim Cosmochim Acta 73:4761–4791. <https://doi.org/10.1016/j.gca.2009.05.045>
- Cook N, Etschmann B, Ciobanu C, Geraki K, Howard D, Williams T, Rae N, Pring A, Chen G, Johannessen B, Brugger J (2015) Distribution and substitution mechanism of Ge in a Ge-(Fe)-bearing sphalerite. Minerals 5:117–132. <https://doi.org/10.3390/min5020117>
- Couderc JJ, Dudouit I, Hennig-Michaeli C, Levade C (1985) The interaction between slip and twinning systems in natural sphalerite experimentally deformed. Phys Status Solidi 90:581–593. <https://doi.org/10.1002/pssa.2210900222>
- Cox SF (1987) Flow mechanisms in sulphide minerals. Ore Geol Rev 2:133–171
- Cugerone A, Cenki-Tok B, Chauvet A, Le Goff E, Bailly L, Alard O, Allard M (2018a) Relationships between the occurrence of accessory Ge-minerals

and sphalerite in Variscan Pb-Zn deposits of the Bossost anticlinorium, French Pyrenean Axial Zone: chemistry, microstructures and ore-deposit setting. *Ore Geol Rev* 95:1–19.

<https://doi.org/10.1016/j.oregeorev.2018.02.016>

Cugerone A, Oliot E, Chauvet A, Gavalda J, Le Goff E (2018b) Structural control on the formation of Pb-Zn deposits: an example from the Pyrenean Axial Zone. *Minerals* 8:1–20. <https://doi.org/10.3390/min8110489>

Cugerone A, Cenki-tok B, Oliot E, Muñoz M, Barou F, Motto-Ros V, Le Goff E (2019) Redistribution of germanium during dynamic recrystallization of sphalerite. *Geology* 48:236–241. <https://doi.org/10.1130/G46791.1>

de Hoÿm de Marien L, Le Bayon B, Pitra P, Van Den Driessche J, Poujol M, Cagnard F (2019) Two-stage Variscan metamorphism in the Canigou massif: evidence for crustal thickening in the Pyrenees. *J Metamorph Geol* 37:1–26. <https://doi.org/10.1111/jmg.12487>

Denèle Y, Laumonier B, Paquette J-L, Olivier P, Gleizes G, Barbey P (2014) Timing of granite emplacement, crustal flow and gneiss dome formation in the Variscan segment of the Pyrenees. Schulmann, K, al, eds, *Variscan Orogeny Extent, Timescale Form Eur Crust Geol Soc London, Spec Publ* 405:265–287. <https://doi.org/10.1144/SP405.5>

Dubosq R, Lawley CJM, Rogowitz A, Schneider DA, Jackson S (2018) Pyrite deformation and connections to gold mobility: insight from micro-structural analysis and trace element mapping. *Lithos* 310–311:86–104. <https://doi.org/10.1016/j.lithos.2018.03.024>

Emslie DP (1960) The mineralogy and geochemistry of the copper, lead, and zinc sulphides of the Otavi Mountainland. *Rep Natl Inst Metall*:1–52

European Commission (2017) Study on the review of the list of critical raw materials criticality assessments. *Eur Comm - Final Rep*:1–93

Fabre C, Devismes D, Moncayo S, Pelascini F, Trichard F, Lecomte A, Bousquet B, Cauzid J, Motto-Ros V (2018) Elemental imaging by laser-induced breakdown spectroscopy for the geological characterization of minerals. *J Anal At Spectrom R Soc Chem*:1–9. <https://doi.org/10.1039/c8ja00048d>

Fougerouse D, Micklethwaite S, Tomkins AG, Mei Y, Kilburn M, Guagliardo P, Fisher LA, Halfpenny A, Gee M, Paterson D, Howard DL (2016) Gold remobilisation and formation of high grade ore shoots driven by dissolution-reprecipitation replacement and Ni substitution into auriferous arsenopyrite. *Geochim Cosmochim Acta* 178:143–159.

<https://doi.org/10.1016/j.gca.2016.01.040>

Francotte J, Moreau J, Ottenburgs R, Levy C (1965) La briartite, une nouvelle espèce minérale. *Bull Soc Fr Minéral Cristallogr* 88:432–437

Frenzel M, Ketris MP, Gutzmer J (2014) On the geological availability of germanium. *Mineral Deposits* 49:471–486. <https://doi.org/10.1007/s00126-013-0506-z>

Frenzel M, Hirsch T, Gutzmer J (2016) Gallium, germanium, indium, and other trace and minor elements in sphalerite as a function of deposit type - a meta-analysis. *Ore Geol Rev* 76:52–78.

<https://doi.org/10.1016/j.oregeorev.2015.12.017>

Frenzel M, Mikolajczak C, Reuter MA, Gutzmer J (2017) Quantifying the relative availability of high-tech by-product metals – the cases of gallium, germanium and indium. *Res Policy* 52:327–335.

<https://doi.org/10.1016/j.resourpol.2017.04.008>

George LL, Cook NJ, Ciobanu CL (2016) Partitioning of trace elements in co-crystallized sphalerite-galena-chalcopyrite hydrothermal ores. *Ore Geol Rev* 77:97–116. <https://doi.org/10.1016/j.oregeorev.2016.02.009>

Gibson GM, Hutton LJ, Holzschuh J (2017) Basin inversion and supercontinent assembly as drivers of sediment-hosted Pb–Zn mineralization in the Mount Isa region, northern Australia. *J Geol Soc Lond* 174:jgs2016–jgs2105. <https://doi.org/10.1144/jgs2016-105>

Goffin V, Evrard M, Pirard E (2015) Critical metals in sphalerites from Belgian MVT deposits. *Proc 13th SGA Bienn Meet* 1–4

Hack AC, Mavrogenes JA (2006) A synthetic fluid inclusion study of copper solubility in hydrothermal brines from 525 to 725 °C and 0.3 to 1.7 GPa. *Geochim Cosmochim Acta* 70:3970–3985.

<https://doi.org/10.1016/j.gca.2006.04.035>

Han R-S, Liu C-Q, Huang Z-L, Chen J, Ma D-Y, Lei L, Ma G-S (2006) Geological features and origin of the Huize carbonate-hosted Zn–Pb–(Ag) District, Yunnan, South China. *Ore Geol Rev* 31:360–383.
<https://doi.org/10.1016/j.oregeorev.2006.03.003>

Henjes-Kunst E, Raith JG, Boyce AJ (2017) Micro-scale sulfur isotope and chemical variations in sphalerite from the Bleiberg Pb-Zn deposit, Eastern Alps, Austria. *Ore Geol Rev* 90:52–62.
<https://doi.org/10.1016/j.oregeorev.2017.10.020>

Höll R, Kling M, Schroll E (2007) Metallogenesis of germanium—a review. *Ore Geol Rev* 30:145–180. <https://doi.org/10.1016/j.oregeorev.2005.07.034>

Horn S, Dziggel A, Kolb J, Sindern S (2018) Textural characteristics and trace element distribution in carbonate-hosted Zn-Pb-Ag ores at the Paleoproterozoic Black Angel deposit, central West Greenland. *Mineral Deposits* 54:507–524. <https://doi.org/10.1007/s00126-018-0821-5>

Hughes MJ (1987) The Tsumeb ore body, Namibia, and related dolostone-hosted base metal ore deposits of Central Africa. Ph D Thesis Univ Witwatersrand, Johannesburg p448

Huston DL, Stevens B, Southgate PN, Muhling P, Wyborn L (2006) Australian Zn-Pb-Ag ore-forming systems: a review and analysis. *Econ Geol* 101:1117–1157. <https://doi.org/10.2113/gsecongeo.101.6.1117>

Johan Z (1988) Indium and germanium in the structure of sphalerite: an example of coupled substitution with copper. *Mineral Petrol* 39:211–229.
<https://doi.org/10.1007/BF01163036>

Johan Z, Oudin E (1986) Présence de grenats, $\text{Ca}_3\text{Ga}(\text{GeO}_4)_3$, $\text{Ca}_3\text{Al}_2[(\text{Ge},\text{Si})\text{O}_4]_3$ et d'un équivalent ferrifère, germanifère et gallifère de la sapphirine, $\text{Fe}_4(\text{Ga},\text{Sn},\text{Fe})_4(\text{Ga},\text{Ge})_6\text{O}_{20}$, dans la blende des gisements de la zone axiale pyrénéenne. Conditions de formation des. *CR Acad Sc Paris* 9:811–816

Johan Z, Oudin E, Picot P (1983) Analogues germanifères et gallifères des silicates et oxydes dans les gisements de zinc des Pyrénées centrales, France; argutite et carboirite, deux nouvelles espèces minérales. *TMPM Tschermaks Mineral und Petrogr Mitteilungen* 31:97–119.
<https://doi.org/10.1007/BF01084764>

Johnson CA, Cardellach E, Tritlla J, Hanan BB (1996) Cierco Pb-Zn-Ag vein deposits: isotopic and fluid inclusion evidence for formation during the mesozoic extension in the pyrenees of Spain. *Econ Geol* 91:497–506. <https://doi.org/10.5962/bhl.title.18736>

Julliot JY, Volfinger M, Robert JL (1987) Mineralogy petrology experimental study of carboirite and related phases in the system $\text{GeO}_2\text{-SiO}_2\text{-Al}_2\text{O}_3\text{-FeO-H}_2\text{O}$ at P up to 2 kbar. *Mineral Petrol* 36:51–69

Kamona AF, Friedrich GH (2007) Geology, mineralogy and stable isotope geochemistry of the Kabwe carbonate-hosted Pb-Zn deposit, Central Zambia. *Ore Geol Rev* 30:217–243. <https://doi.org/10.1016/j.oregeorev.2006.02.003>

Kampmann TC, Jansson NF, Stephens MB, Olin PH, Gilbert S, Wanhainen C (2018) Syn-tectonic sulphide remobilization and trace element redistribution at the Falun pyritic Zn-Pb-Cu-(Au-Ag) sulphide deposit, Bergslagen, Sweden. *Ore Geol Rev* 96:48–71. <https://doi.org/10.1016/j.oregeorev.2018.04.010>

Kampunzu AB, Cailteux JLH, Kamona AF, Intiomale MM, Melcher F (2009) Sediment-hosted Zn-Pb-Cu deposits in the Central African Copperbelt. *Ore Geol Rev* 35:263–297. <https://doi.org/10.1016/j.oregeorev.2009.02.003>

Kelley KD, Jennings S (2004) A special issue devoted to barite and Zn-Pb-Ag deposits in the Red Dog district, Western Brooks Range, northern Alaska. *Econ Geol* 99:1267–1280. <https://doi.org/10.2113/gsecongeo.99.7.1267>

Kleinsmiede WFJ (1960) Geology of the Valle de Aran (Central Pyrenees). *Leidse Geol Meded* 25:129–245

Klinger L, Rabkin E (1999) Beyond the Fisher model of grain boundary diffusion: effect of structural inhomogeneity in the bulk. *Acta Mater* 47:725–734. [https://doi.org/10.1016/S1359-6454\(98\)00420-0](https://doi.org/10.1016/S1359-6454(98)00420-0)

Laforet C, Oudin E, Picot P, Pierrot R, Pillard F (1981) Métallogénie régionale: Utilisation des paragenèses minéralogiques et des minéraux traceurs. *Bur Rech Geol Minieres Rapp* 80 SGN175:33p

Large RR, Bull SW, McGoldrick PJ, Walters S, Derrick GM, Carr GR (2005) Stratiform and strata-bound Zn-Pb-Ag deposits in proterozoic sedimentary basins, Northern Australia. *Econ Geol* 100th Anniv Vol 931–963

Large RR, Danyushevsky L, Hollit C, Maslennikov V, Meffre S, Gilbert S, Bull S, Scott R, Emsbo P, Thomas H, Singh B, Foster J (2009) Gold and trace element zonation in pyrite using a laser imaging technique: implications for the timing of gold in orogenic and carlin-style sediment-hosted deposits. *Econ Geol* 104:635–668

Laumonier B, Marignac C, Kister P (2010) Polymétamorphisme et évolution crustale dans les Pyrénées orientales pendant l'orogénèse varisque au Carbonifère supérieur. *Bull la Société géologique Fr* 181:411–428

Lawrence LJ (1973) Polymetamorphism of the sulphide ores of Broken Hill, NSW, Australia. *Mineral Deposits* 8:211–236

Licht C, Peiró LT, Villalba G (2015) Global substance flow analysis of gallium, germanium, and indium: quantification of extraction, uses, and dissipative losses within their anthropogenic cycles. *J Ind Ecol* 19:890–903. <https://doi.org/10.1111/jiec.12287>

Lockington JA, Cook NJ, Ciobanu CL (2014) Trace and minor elements in sphalerite from metamorphosed sulphide deposits. *Mineral Petrol* 108:873–890. <https://doi.org/10.1007/s00710-014-0346-2>

Melcher F, Onuk P (2019) Potential of critical high-technology metals in eastern alpine base metal sulfide ores. *Berg- und Hüttenmännische Monatshefte* 164:1–6. <https://doi.org/10.1007/s00501-018-0818-5>

Melcher F, Oberthür T, Rammlmair D (2006) Geochemical and mineralogical distribution of germanium in the Khusib Springs Cu-Zn-Pb-Ag sulfide deposit, Otavi Mountain Land, Namibia. *Ore Geol Rev* 28:32–56. <https://doi.org/10.1016/j.oregeorev.2005.04.006>

Mezger JE, Passchier CW (2003) Polymetamorphism and ductile deformation of staurolite–cordierite schist of the Bossòst dome: indication for Variscan extension in the Axial Zone of the central Pyrenees. *Geol Mag* 140:595–612. <https://doi.org/10.1017/S0016756803008112>

Mezger JE, Passchier CW, Régnier J-L (2004) Metastable staurolite–cordierite assemblage of the Bossòst dome: late Variscan decompression and polyphase metamorphism in the Axial Zone of the central Pyrenees. *Compt Rendus Geosci* 336:827–837. <https://doi.org/10.1016/j.crte.2003.12.024>

Monteiro SLV, Bettencourt SJ, Juliani C, de Oliveira TF (2006) Geology, petrography, and mineral chemistry of the Vazante non-sulfide and Ambrosia and Fagundes sulfide-rich carbonate-hosted Zn–(Pb) deposits, Minas Gerais, Brazil. *Ore Geol Rev* 28:201–234.

<https://doi.org/10.1016/j.oregeorev.2005.03.005>

Moore DW, Young LE, Modene JS, Plahuta JT (1986) Geologic setting and genesis of the Red Dog zinc-lead-silver deposit, western Brooks Range, Alaska. *Econ Geol* 81:1696–1727.

<https://doi.org/10.2113/gsecongeo.81.7.1696>

Munoz M, Boyce AJ, Courjault-Rade P, Fallick AE, Tollon F (1994) Multi-stage fluid incursion in the Palaeozoic basement-hosted Saint-Salvy ore deposit (NW Montagne Noire, southern France). *Appl Geochem* 9:609–626.

[https://doi.org/10.1016/0883-2927\(94\)90022-1](https://doi.org/10.1016/0883-2927(94)90022-1)

Murakami H, Ishihara S (2013) Trace elements of indium-bearing sphalerite from tin-polymetallic deposits in Bolivia, China and Japan: a femto-second LA-ICPMS study. *Ore Geol Rev* 53:223–243.

<https://doi.org/10.1016/j.oregeorev.2013.01.010>

Murphy TE (2004) Structural and stratigraphic controls on mineralization at the George Fisher Zn-Pb-Ag deposit, Northwest Queensland, Australia. Ph D Thesis, James Cook Univ 1–423

~~Oliveira JT, Pereira Z, Carvalho P, Pacheco N, Korn D (2004) Stratigraphy of the tectonically imbricated lithological succession of the Neves Corvo mine area, Iberian Pyrite Belt, Portugal. *Mineral Deposits* 39:422–436.~~

~~<https://doi.org/10.1007/s00126-004-0415-2>~~

~~Ostendorf J, Henjes-Kunst F, Schneider J, Melcher F, Gutzmer J (2017) Genesis of the carbonate-hosted Tres Marias Zn-Pb-(Ge) deposit, Mexico: constraints from Rb-Sr sphalerite geochronology and Pb isotopes. *Econ Geol* 112:1075–1087. <https://doi.org/10.5382/econgeo.2017.4502>~~

Ottemann VJ, Nuber B (1972) Brunogeierit, ein Germanium-Ferritspinell von Tsumeb. *Neues Jahrb Mineral Monatshefte*:263–267

Ovejero Zappino G (1991) Mineralizaciones Zn-Pb ordovícicas del anticlinorio de Bossost. Yacimientos de Liat y Victoria. Valle de Arán. Pirineo (España). *Bol Geol Min* 102–3:356–377

Pearce NJG, Perkins WT, Westgate JA, Jackson SE, Neal CR, Chenery SP, Gorton MP (1997) A compilation of new and published major and trace element data for NIST SRM 610 and NIST SRM 612 glass reference materials. *Geostand Newslett* 21:1–30

Plümper O, King HE, Vollmer C, Ramasse Q, Jung H, Austrheim H (2012) The legacy of crystal-plastic deformation in olivine: high-diffusivity pathways during serpentinization. *Contrib Mineral Petrol* 163:701–724. <https://doi.org/10.1007/s00410-011-0695-3>

Pokrovski GS, Schott J (1998) Thermodynamic properties of aqueous Ge(IV) hydroxide complexes from 25 to 350°C: implications for the behavior of germanium and the Ge/Si ratio in hydrothermal fluids. *Geochim Cosmochim Acta* 62:1631–1642

Pokrovski GS, Roux J, Hazemann JL, Testemale D (2005) An X-ray absorption spectroscopy study of argutite solubility and aqueous Ge(IV) speciation in hydrothermal fluids to 500 °C and 400 bar. *Chem Geol* 217:127–145. <https://doi.org/10.1016/j.chemgeo.2005.01.006>

Pouit G (1985) Les minéralisations Zn (Pb) Ba du Paléozoïque des Pyrénées Centrales : Une mise au point et un compte rendu des missions 1984. *Bur Rech Géologiques Minières Rapp* 85 DAM037:72

Pouit G, Bois JP (1986) Arrens Zn (Pb), Ba Devonian deposit, Pyrénées, France: an exhalative-sedimentary-type deposit similar to Meggen. *Mineral Deposits* 21:181–189

Reddy SM, Hough RM (2013) Microstructural evolution and trace element mobility in Witwatersrand pyrite. *Contrib Mineral Petrol* 166:1269–1284. <https://doi.org/10.1007/s00410-013-0925-y>

Reddy SM, Timms NE, Pantleon W, Trimby P (2007) Quantitative characterization of plastic deformation of zircon and geological implications. *Contrib Mineral Petrol* 153:625–645. <https://doi.org/10.1007/s00410-006-0174-4>

Reiser FKM, Rosa DRN, Pinto ãMM, Carvalho JRS, Matos JX, Guimaraes FMG, Alves LC, de Oliveira DPS (2011) Mineralogy and geochemistry of tin- and germanium-bearing copper ore, Barrigao re-mobilized vein deposit, Iberian Pyrite Belt, Portugal. *Int Geol Rev* 53:1212–1238. <https://doi.org/10.1080/00206811003683168>

Relvas JMRS, Barriga FJAS, Longstaffe FJ (2006) Hydrothermal alteration and mineralization in the Neves-Corvo volcanic-hosted massive sulfide deposit, Portugal. II. Oxygen, hydrogen, and carbon isotopes. *Econ Geol* 101:791–804. <https://doi.org/10.2113/gsecongeo.101.4.791>

Ruiz AG, Sola PC, Palmerola NM (2018) Germanium: current and novel recovery processes. Lee, S, ed, *Adv Mater Device Appl with Ger* London, IntechOpen Ltd Chapter 2:p.9–29.
<https://doi.org/10.5772/INTECHOPEN.77997>

Sahlström F, Arribas A, Dirks P, Corral I, Chang Z (2017) Mineralogical distribution of germanium, gallium and indium at the Mt Carlton high-sulfidation epithermal deposit, NE Australia, and comparison with similar deposits worldwide. *Minerals* 7:213. <https://doi.org/10.3390/min7110213>

Saini-Eidukat B, Melcher F, Lodziak J (2009) Zinc-germanium ores of the Tres Marias Mine, Chihuahua, Mexico. *Mineral Deposits* 44:363–370.
<https://doi.org/10.1007/s00126-008-0222-2>

Sancey L, Motto-Ros V, Busser B, Kotb S, Benoit JM, Piednoir A, Lux F, Tillement O, Panczer G, Yu J (2014) Laser spectrometry for multi-elemental imaging of biological tissues. *Sci Rep* 4:1–8.
<https://doi.org/10.1038/srep06065>

Shannon R (1976) Revised effective ionic radii and systematic studies of interatomic distances in Halides and Chalcogenides. *Acta Cryst* 32:751–767

Siemes H, Borges B (1979) Experimental deformation of sphalerite single crystals under confining pressures of 3000 and 5000 bars at temperatures between 25°C and 450°C. *N Jb Miner Abb* 134:288–304

Spry PG, Plimer IR, Teale GS (2008) Did the giant Broken Hill (Australia) Zn-Pb-Ag deposit melt? *Ore Geol Rev* 34:223–241.
<https://doi.org/10.1016/j.oregeorev.2007.11.001>

Tomkins AG, Mavrogenes JA (2001) Redistribution of gold within arsenopyrite and löllingite during pro- and retrograde metamorphism: application to timing of mineralization. *Econ Geol* 96:525–534.
<https://doi.org/10.2113/gsecongeo.96.3.525>

U.S. Geological Survey (2019) Mineral commodity summaries 2019

Van Achterbergh E, Ryan CG, Griffin WL (2001) Glitter! User's manual on-line interact data reduct LA-ICPMS microprobe 1–72

Velásquez G, Béziat D, Salvi S, Siebenaller L, Borisova AY, Pokrovski GS, De Parseval P (2014) Formation and deformation of pyrite and implications for gold mineralization in the El Callao District, Venezuela. *Econ Geol* 109:457–486. <https://doi.org/10.2113/econgeo.109.2.457>

Viets J, Hopkins R, Miller B (1992) Variations in minor and trace metals in sphalerite from Mississippi Valley-type deposits of the Ozark region: genetic implications. *Econ Geol* 87:1897–1905

Vikentyev IV, Belogub EV, Novoselov KA, Moloshag VP (2016) Metamorphism of volcanogenic massive sulphide deposits in the Urals. *Ore Geol Ore Geol Rev* 34:30–63. <https://doi.org/10.1016/j.oregeorev.2016.10.032>

Villars P, Calvert LD (1991) Pearson's handbook of crystallographic data for intermetallic phases

Vukmanovic Z, Reddy SM, Godel B, Barnes SJ, Fiorentini ML, Barnes SJ, Kilburn MR (2014) Relationship between microstructures and grain-scale trace element distribution in komatiite-hosted magmatic sulphide ores. *Lithos* 184–187:42–61. <https://doi.org/10.1016/j.lithos.2013.10.037>

Wagner T, Monecke T (2005) Germanium-bearing colusite from the Waterloo volcanic-rock-hosted massive sulfide deposit, Australia: crystal chemistry and formation of colusite-group minerals. *Can Mineral* 43:655–669. <https://doi.org/10.2113/gscanmin.43.2.655>

Wagner T, Klemd R, Wenzel T, Mattsson B (2007) Gold upgrading in metamorphosed massive sulfide ore deposits: direct evidence from laser-ablation-inductively coupled plasma-mass spectrometry analysis of invisible gold. *Geology* 35:775–778. <https://doi.org/10.1130/G23739A.1>

Wei C, Huang Z, Yan Z, Hu Y, Ye L (2018) Trace element contents in sphalerite from the Nayongzhi Zn-Pb deposit, northwestern Guizhou, China: insights into incorporation mechanisms, metallogenic temperature and ore genesis. *Minerals* 8:490. <https://doi.org/10.3390/min8110490>

Wei C, Ye L, Hu Y, Danyushevskiy L, Li Z, Huang Z (2019) Distribution and occurrence of Ge and related trace elements in sphalerite from the Lehong

carbonate-hosted Zn-Pb deposit, northeastern Yunnan, China: insights from SEM and LA-ICP-MS studies. *Ore Geol Rev* 115:103175.

<https://doi.org/10.1016/j.oregeorev.2019.103175>

Wilkinson JJ (2013) Sediment-hosted zinc-lead mineralization: processes and perspectives, treatise on geochemistry, Second Edition. Elsevier, H Holland, K Turekian (ed), Amsterdam, Netherlands 219–249.

<https://doi.org/10.1016/B978-0-08-095975-7.01109-8>

Wilson SA, Ridley WI, Koenig AE (2002) Development of sulfide calibration standards for the laser ablation inductively-coupled plasma mass spectrometry technique. *J Anal At Spectrom* 17:406–409.

<https://doi.org/10.1039/b108787h>

Xue C, Zeng R, Liu S, Chi G, Qing H, Chen Y, Yang J, Wang D (2007) Geologic, fluid inclusion and isotopic characteristics of the Jinding Zn-Pb deposit, western Yunnan, South China: a review. *Ore Geol Rev* 31:337–359.

<https://doi.org/10.1016/j.oregeorev.2005.04.007>

Ye L, Tiegeng L (1999) Sphalerite chemistry, Niujiaotang Cd-rich zinc deposit, Guizhou, Southwest China. *Chin J Geochem* 18:62–68

Ye L, Cook NJ, Ciobanu CL, Yuping L, Qian Z, Tiegeng L, Wei G, Yulong Y, Danyushevskiy L (2011) Trace and minor elements in sphalerite from base metal deposits in South China: a LA-ICPMS study. *Ore Geol Rev* 39:188–217.

<https://doi.org/10.1016/j.oregeorev.2011.03.001>

Ye L, Cook NJ, Liu T, Ciobanu CL, Gao W, Yang Y (2012) The Niujiaotang Cd-rich zinc deposit, Duyun, Guizhou province, Southwest China: ore genesis and mechanisms of cadmium concentration. *Mineral Deposits* 47:683–700.

<https://doi.org/10.1007/s00126-011-0386-z>

Zwart HJ (1963) Metamorphic history of the Central Pyrenees, part II, Valle de Aran. *Leidse Geol Meded* 28:321–376

Zwart HJ (1979) The geology of the Central Pyrenees. *Leidse Geol Meded* 50:1–74